ACCSCIENCE PUBLISHING

OR

ORIGINAL RESEARCH ARTICLE

Bone organoid–derived extracellular vesicles promote angiogenesis and osteogenesis *in vitro*

Zhenning Dai[1†], Ding Li[2†], Hui Lu[3†], Suiqing Huang[4†], Jiarui Liu[5], Jingyuan Huang[5], Ruoqi Ma[5], Wenqiang Zhou[6], Weiwei Su[7]*, Wengang Liu[1]*, Shiyu Li[5]*, and Guobing Chen[5]*

[1]Guangdong Provincial Key Laboratory of Research and Development in Traditional Chinese Medicine, Guangdong Provincial Second Hospital of Traditional Chinese Medicine, Guangzhou, Guangdong, China

[2]School of Fashion, Guangdong Polytechnic, Foshan, Guangdong, China

[3]Institute of Translational Medicine, Shanghai University, Shanghai, China

[4]Department of Cardiac Surgery, First Affiliated Hospital of Sun Yat-sen University, Guangzhou, Guangdong, China

[5]Department of Immunology, School of Medicine, Jinan University, Guangzhou, Guangdong, China

[6]Department of Intensive Care Unit, The First Affiliated Hospital of Jinan University, Guangzhou, Guangdong, China

[7]Department of Minimally Invasive Spinal Surgery, The Affiliated Hospital of Putian University, Putian, Fujian, China

***Corresponding authors:** Guobing Chen (guobingchen@jnu.edu.cn); Shiyu Li (lishiyu@jnu.edu.cn); Wengang Liu (914194079@qq.com); Weiwei Su (suweiwei@ptu.edu.cn)

[†]*These authors contributed equally to this work.*

Citation: Dai Z, Li D, Huang S, *et al*. Bone organoid–derived extracellular vesicles promote angiogenesis and osteogenesis *in vitro*. *Organoid Res.* 2026;2(3):026140021. doi: 10.36922/OR026140021

Received: April 2, 2026

Revised: July 21, 2026

Accepted: August 5, 2026

Published online: September 18, 2026

Copyright: © 2026 Author(s). This is an Open-Access article distributed under the terms of the Creative Commons Attribution License, permitting distribution, and reproduction in any medium, which provided that the original work is properly cited.

Publisher's Note: AccScience Publishing remains neutral with regard to jurisdictional claims in published maps and institutional affiliations.

Abstract

Bone organoids (BOs) demonstrate excellent therapeutic effects in bone defect transplantation, but their high cultivation difficulty and cost limit widespread adoption, prompting us to focus on their derivatives. Whether BO-derived extracellular vesicles (BOEVs) can promote bone regeneration and whether they offer greater advantages than stem cell-derived extracellular vesicles (EVs) remains unclear. In this study, we isolated rat bone marrow mesenchymal stem cells (BMSCs) and induced them into BOs. As culture duration increased, BO size gradually enlarged to 203.71 ± 45.30 μm, but the number of spheroids progressively decreased. Messenger RNA (mRNA) sequencing revealed that after seven days of culture, BOs exhibited hypoxic alterations, leading to increased expression of cytokines, including hypoxia-inducible factor-1α (HIF-1α). Subsequently, BOEVs were isolated from BO culture medium at corresponding time points. Both BOEVs cultured for seven days (BOEV-7d) and 14 days (BOEV-14d) were enriched with bone morphogenetic protein 2 (BMP-2), transforming growth factor beta 1 (TGF-β1), HIF-1α, and vascular endothelial growth factor (VEGF). Co-culturing BOEVs with human umbilical vein endothelial cells and hFOB1.19 cells revealed that BOEV-7d significantly promoted tube length and branching while upregulating *VEGF* and *CCN2* mRNA, demonstrating superior effects compared to BOEV-1d and BOEV-14d. Concurrently, BOEV-7d enhanced alizarin red S staining levels in hFOB1.19 cells, while the expression of osteogenesis-related genes *Runx2*, *Col1a1*, and *Ocn* was positively correlated with culture duration. Notably, BOEVs demonstrated significantly greater osteogenic and angiogenic effects than BMSC-derived EVs in 2D culture. This study demonstrates, in vitro, that BOEVs play dual roles in bone and vascular regeneration and have the potential to modulate the vascularization–osteogenesis pathway in bone defects. It offers insights into bone defect treatment and inspires research on organoid-derived EVs.

Keywords: Bone organoid; Extracellular vesicles; Hypoxia; Angiogenesis; Osteogenic differentiation

1. Introduction

The regeneration of bone defects caused by trauma, infection, tumors, or inherent genetic disorders represents a global clinical challenge.[1] Over 10 million bone graft procedures are performed annually, with this figure continuing to grow at a rate of 10% per year.[2,3] Alternative approaches for repairing substantial bone defects in clinical practice—such as metal implants, allografts, and artificial grafts—carry drawbacks, including limited donor-site availability, risks of disease transmission, and suboptimal osseointegration outcomes.[4,5] Consequently, these strategies fall short as optimal treatments for bone regeneration, necessitating more effective approaches to enhance bone regeneration and accelerate healing. With advances in regenerative medicine, organoid technology has emerged as a promising solution and garnered significant attention.[6] Organoids are 3D cell clusters cultured from stem cells using *in vitro* 3D culture techniques. Possessing self-renewal and self-organization capabilities, organoids constitute a class of microphysiological systems that exhibit spatial structures and physiological functions similar to those of their source tissues.[7] Culturing organoids from stem cells derived from healthy/diseased tissues can recapitulate source tissue characteristics, offering opportunities to investigate the growth mechanisms of these tissues.[8,9]

Bone organoids (BOs) are 3D, miniaturized, and simplified versions of bone tissue created *in vitro* using stem cells or progenitor cells.[10,11] These organoids are meticulously engineered to mimic the structure, function, and cellular complexity of natural bone tissue, including key features such as mineralization and vascularization.[12] In a recent study by Wang *et al.*[13], large-scale self-mineralizing BOs were constructed via 3D bioprinting using a gelatin methacrylate (GelMA)/alginate methacrylate (AlgMA)/hydroxyapatite (HAp) composite bioink. These BOs demonstrated excellent cell viability, self-mineralization capacity, and multicellular differentiation potential in both *in vitro* and *in vivo* cultures. However, as 3D tissue models, organoids often exhibit hypoxia in their central regions as their volume increases[14,15], making hypoxia a key factor limiting organoid growth and maturation. Central hypoxia primarily stems from restricted diffusion of oxygen and nutrients within organelles, leaving central cells in hypoxic or even anoxic conditions. These conditions trigger apoptosis and necrosis, compromising overall organoid function and stability. Studies have indicated that central hypoxia alters cellular metabolism, activates the hypoxia-inducible factor (HIF) signaling pathway, and regulates proliferation, differentiation, and metabolic reprogramming.[16] For example, during brain organoid culture, HIF-1α expression frequently emerges in the central zone, accompanied by cell necrosis and functional impairment, limiting long-term culture and maturation.[17] Therefore, as BOs grow and develop, the central cells will also undergo hypoxia-induced necrosis.[18] In summary, BO research represents a major shift in regenerative medicine, addressing challenges in bone defect repair, hematopoietic niche reconstruction, and vascularization.[1,19] However, traditional organoid construction typically relies on natural matrix gels derived from mice (such as Matrigel), which present drawbacks such as high cost, unclear composition, batch-to-batch variability, and high immunogenicity.[20,21] Do organoid-derived extracellular vesicles (EVs) also possess tissue repair-promoting effects? How does central hypoxia-induced necrosis in organoids affect their EV functions? In this study, we focused on BO-derived EVs (BOEVs).

Extracellular vesicles, with diameters ranging from 30 to 150 nm, are widely secreted by various cell types and participate in intercellular signaling.[22,23] While their functional diversity extends far beyond this canonical role, they also act as cellular waste transporters and key mineral inducers, especially in bone remodeling, and can interact with the extracellular matrix to regulate tissue microenvironment homeostasis. Notably, EVs are frequently co-purified with non-vesicular nanoparticles during isolation procedures, and these nanoparticles have been reported to carry higher abundances of proteins and nucleic acids than EVs, necessitating rigorous validation to distinguish the biological effects of EVs from those of co-purified non-vesicular nanoparticles in related functional studies. In bone tissue repair, EV-mediated intercellular communication is considered one of the key mechanisms regulating osteocyte function and promoting bone regeneration. *In vitro* studies have demonstrated that EVs derived from human umbilical cord mesenchymal stem cells significantly enhance the proliferation, migration, and osteogenic differentiation of osteoprogenitor cells. Given the promising outcomes of BOs in bone regeneration and defect filling, BOEVs warrant greater attention.[24] Theoretically, these EVs could also exert bone-regenerative effects and reflect the growth and developmental status of BOs, though no such reports have been published to date. In traditional 2D culture, cell contacts occur only on a single plane. In contrast, organoids form self-organized 3D cell clusters *in vitro*, making cell contacts more analogous to those *in vivo*.[24] Importantly, organoid-derived EVs exhibit 96% RNA similarity to serum-derived EVs.[9] Subsequent culture studies have also revealed that EVs collected from 3D cultures are 1.5–4.5 times more abundant than those from 2D cultures.[25] Consequently, organoid-derived EVs are proposed to have superior physiological and therapeutic potential compared to conventional EVs.[25,26]

Therefore, this work is dedicated to exploring the therapeutic effects of BOEVs on bone defects and their underlying mechanisms. We aim to create rat bone marrow mesenchymal stem cell (BMSC) BOs, group them

by culture duration during osteogenic induction, and extract BOEVs. Through transcriptomic analysis, EV–cell co-culture experiments, and animal validation studies, we aim to clarify how the duration of organoid culture influences the proteomic composition of EVs. We seek to elucidate the role of BOEVs in reflecting BO growth states—such as osteogenic differentiation, internal hypoxia, and apoptosis—and investigate the therapeutic potential of BOEVs in promoting osteogenic differentiation. This research will provide novel insights into the diagnosis and treatment of bone disorders.

2. Methods

2.1. Cell culture

Following ethical guidelines for laboratory animal care, five two-week-old male Sprague–Dawley rats were anesthetized via intraperitoneal injection of an overdose of 3% sodium pentobarbital (150 mg/kg) and immersed in 75% ethanol for 5 min for disinfection. Under aseptic conditions, the tibia and femur were resected, and bone marrow tissue was flushed to obtain a cell suspension. After adding red cell lysis buffer and incubating for 5 min, the suspension was centrifuged at 600×*g*. Cells were cultured for 24 h in Dulbecco's Modified Eagle Medium (DMEM; Gibco, United States of America [USA]) supplemented with 10% exosome-free fetal bovine serum (EXO-FBS-50A-1, System Biosciences, USA) and 1% penicillin–streptomycin (10,000 U/mL, Gibco). Purified BMSCs were obtained after medium exchange; the medium was changed every two days thereafter. After passaging to the third generation, BMSCs were harvested for subsequent experiments and cultured in osteogenic induction medium (containing 10 mM β-glycerophosphate, 50 μM trisodium salt-2-phosphate-*L*-ascorbic acid, and 100 nM dexamethasone; all from Sigma-Aldrich, USA) at 37 °C in a humidified incubator with 5% CO_2, seeded at 5×10^4 cells per well into six-well plates, and the osteogenic induction medium was replaced every three days.

Human umbilical vein endothelial cells (HUVECs) were purchased from American Type Culture Collection (ATCC; USA). To achieve optimal growth, the cell culture medium was supplemented with 10% exosome-free fetal bovine serum, 100 μg/mL streptomycin, and 100 U/mL penicillin. All procedures were conducted in a biosafety cabinet to maintain sterile conditions. In addition, all reagents, including Dulbecco's phosphate-buffered saline (DPBS), culture medium, and 0.25% trypsin, were preheated and prepared in advance. Cells in logarithmic growth phase were washed twice with DPBS, digested with 0.25% trypsin, and neutralized by adding complete culture medium. The obtained cell suspension was then transferred to a 15 mL centrifuge tube, centrifuged at 300×g for 5 min, and the supernatant was discarded. Subsequently, the cells were resuspended, counted, and diluted to the target concentration. They were inoculated onto a culture plate at a density of 3×10^5 cells/plate to lay the foundation for subsequent experimental procedures.

The human osteoblast cell line hFOB1.19 was purchased from ATCC and cultured in DMEM containing 10% exosome-free fetal bovine serum and 1% penicillin–streptomycin (10,000 U/mL) at 37 °C in a 5% CO_2 incubator. The culture medium was changed every 2–3 days. When cell fusion reached 80%–90%, the cells were digested with 0.25% trypsin–ethylenediaminetetraacetic acid (EDTA) (Gibco) and passaged. We selected 3–5 passages of cells in the logarithmic growth phase for subsequent osteogenic differentiation-related experiments. To prepare for alizarin red S staining, all reagents, including DPBS, culture medium, osteogenic induction components, and BOEVs, were preheated and prepared under sterile conditions in a biosafety cabinet. Cells were washed twice with pre-warmed DPBS, digested with 0.25% trypsin–EDTA, and neutralized with complete culture medium. The obtained cell suspension was transferred to a 15 mL centrifuge tube, centrifuged at 300×g for 5 m, and the supernatant was discarded. Subsequently, the cells were resuspended, counted, and adjusted to a target density of 5×10^4 cells per well. The cell suspension was inoculated into six-well plates and cultured in complete medium for 24 h to allow adherence, laying the foundation for subsequent alizarin red S staining experiments.

2.2. Characterization of bone marrow mesenchymal stem cells

Flow cytometry was conducted to identify the surface immunophenotypic markers of BMSCs. Briefly, BMSCs in the logarithmic growth phase were harvested and adjusted to 3.5×10^5 cells per tube with pre-chilled phosphate-buffered saline (PBS). The cells were incubated with specific fluorescent-conjugated antibodies for 30 min in the dark at room temperature, including CD73-phycoerythrin (PE) (130-112-060, Miltenyi Biotec; Germany), CD90-PE (130-114-902, Miltenyi Biotec), CD45-fluorescein isothiocyanate (FITC) (130-119-769, Miltenyi Biotec), and CD34-FITC (130-113-740, Miltenyi Biotec). After incubation, unbound antibodies were removed by two washes with pre-chilled PBS at 300×g for 5 min each. The stained cells were immediately analyzed using a flow cytometer (MACSQuant Analyzer 10, Miltenyi Biotec) to detect BMSC surface marker expression.

2.3. Construction of bone organoids

After seven days of osteogenic induction, BMSCs were digested with 0.25% trypsin-EDTA for 3 min at 37 °C, and the digestion was terminated with complete culture

medium containing 10% exosome-free FBS. The cell suspension was centrifuged at 300×g for 5 min; the supernatant was discarded, and the cell pellet was washed twice with pre-chilled sterile PBS (pH 7.4). After the final wash, the cells were resuspended in osteogenic induction medium and adjusted to a single-cell suspension with a pipette. To prepare BOs, the suspension of osteoblastically induced BMSCs was seeded at a density of 6×10^5 cells/well into ultra-low attachment 3D cell culture plates (Heidolph, Germany). The plates were then placed in a humidified incubator at 37 °C with 5% CO_2 for static suspension culture, without agitation. Under these non-shaken, ultra-low attachment conditions, cells interacted with the 3D microenvironment of the plate, migrated and aggregated spontaneously, and grew within the 3D spatial architecture, forming 3D cell-carrier complexes. Bright-field observation under an inverted phase-contrast microscope (IX73, Olympus, Japan) was performed at 0 h, 12 h, and 24 h post-inoculation to assess cell aggregation and spheroid formation. After 24 h of culture, spherical BO primary structures with intact morphology were observed.

2.4. Scanning electron microscopy

After successful construction of BOs, they were transferred to conventional culture plates for cultivation. The BOs were grouped by culture duration (1, 7, and 14 days; corresponding to the BO-1d, BO-7d, and BO-14d groups, respectively), and their status was observed under an inverted phase-contrast microscope (IX73, Olympus). The BOs were freeze-dried and coated to enhance conductivity. A scanning electron microscope (SEM; S-3000N, Hitachi, Japan) was used to observe the microstructure of these BOs after freeze-drying and gold plating (10 nm thickness) at 5 kV. The processing steps for the *Hif1a* knockdown group were the same. ImageJ v1.8.0 (National Institutes of Health, USA) was used to analyze microsphere particle size and generate detailed particle-size distribution profiles.

2.5. *Hif1a* knockdown

Hif1a knockdown was achieved through RNA interference. Specific small-interfering RNA (siRNA) targeting the rat *Hif1a* gene (4390771, Thermo Fisher Scientific, USA) and non-targeting siRNA were used. Third-passage rat BMSCs were seeded onto six-well plates, and when cell confluence reached 70%, siRNA transfection was conducted using Lipofectamine 3000 reagent (Invitrogen, USA) following the manufacturer's instructions.

2.6. Real-time quantitative polymerase chain reaction

After 48 h of transfection, total cellular RNA was extracted using TRIzol reagent (Becton Dickinson, USA). RNA purity and concentration were evaluated using a NanoDrop 2000 spectrophotometer (Thermo Fisher Scientific), and complementary DNA (cDNA) was synthesized with a reverse transcription kit (4368814, Thermo Fisher Scientific, USA). Quantitative polymerase chain reaction (qPCR) was performed on a real-time (RT)-polymerase chain reaction (PCR) system (CFX96, Bio-Rad, USA) using the SYBR Green PCR Kit (Thermo Fisher Scientific), with *Gapdh* as the internal control. The $2^{-\Delta\Delta Ct}$ method was used to calculate the relative expression level of *Hif1a* for validating knockdown efficiency.

To validate the differentially expressed genes (DEGs) identified in the messenger RNA (mRNA) sequencing analysis, RT-qPCR was performed using primers specifically designed for osteogenic and angiogenic markers (*Runx2*, *Sp7*, *Col1a1*, *Ocn*, *Vegf*, *Ccn2*, *Fn*), a bone-related gene (*Alp*), an EV-related gene (*Rab27a*), and *Hif1a*, with *Gapdh* serving as the internal control. Primer sequences are detailed in Table 1. Thermal cycling conditions were as follows: 95 °C pre-denaturation for 5 min, followed by 40 cycles (95 °C denaturation for 30 s, 60 °C extension for 30 s, and finally 72 °C digestion for 30 s). Relative gene expression levels were calculated using the $2^{-\Delta\Delta Ct}$ method, and statistical analysis was performed to evaluate the effects of scaffolds on osteoblast-related gene expression.

2.7. Messenger RNA sequencing analysis

Culture media from 3D-cultured osteoblasts and 2D osteoblastically induced BMSCs were collected separately. Total RNA was extracted using TRIzol reagent according to the manufacturer's protocol. RNA quality and purity were assessed using a NanoDrop 2000 spectrophotometer and verified by agarose gel electrophoresis to ensure suitability for library construction. High-quality RNA was reverse transcribed into cDNA, followed by cDNA library preparation. High-throughput sequencing was performed on the Illumina NovaSeq 6000 platform (USA). Sequencing data underwent rigorous quality control, reference genome alignment, gene expression quantification, and identification of DEGs. Specifically, DEGs were defined using a stringent threshold of a false discovery rate (FDR)-adjusted *p*-value (*p*.adj) < 0.05 and |log2(fold change)| ≥ 1. For Gene Ontology (GO) and Kyoto Encyclopedia of Genes and Genomes (KEGG) enrichment analyses, the Benjamini–Hochberg FDR method was employed for multiple testing correction. Only GO terms and KEGG pathways with a *p*.adj < 0.05 were considered statistically significantly enriched. Furthermore, the significance levels and enrichment degree of specific pathways were explicitly quantified and reported using exact *p*.adj and enrichment scores (e.g., GeneRatio). Performing GO and KEGG enrichment analyses on key genes revealed core pathways associated with osteogenesis, elucidating the mechanism by which BOs regulate bone formation in 3D culture.

Table 1. Primers used for real-time quantitative polymerase chain reaction

Gene	Primer	Sequence (5' to 3')
Runx2	Forward	GCGGTGCAAACTTTCTCCAG
	Reverse	TGCAGCCTTAAATGACTCGG
Sp7	Forward	CCTCTTGAGAGGAGACGGGA
	Reverse	GGAGAGGAGTCCATTGGTGC
Col1a1	Forward	CATGGCCAAGAAGACATCCC
	Reverse	TGGGTCCCTCGACTCCTATG
Ocn	Forward	GAATAGACTCCGGCGCTACC
	Reverse	TCCTGGAAGCCAATGTGGTC
Gapdh	Forward	AGGTCGGTGTGAACGGATTT
	Reverse	ACCAGCTTCCCATTCTCAGC
Alp	Forward	CTCTGGACTTGGTGGTCACA
	Reverse	ACGTTCCGATCCTGAGTGG
Hif1a	Forward	ACATGGGGTTGACTCAGTTTGA
	Reverse	AAAAGCTTCGCTGCGTGTTT
Rab27a	Forward	AGAGCACCAAACCGGGTAAA
	Reverse	CCTCGGCCTACAGTTCCATC
Vegf	Forward	CAAGCCGTCCTGTGTGCC
	Reverse	TCCAGGGCTTCATCATTGC
Ccn2	Forward	CACCCGAGTTACGAAAACAT
	Reverse	GGCAGGTCTTGATGAACTCC
Fn	Forward	TGATTGGGAGGAAAAAGACAG
	Reverse	CTGTGGAGGGAACATCCAA

2.8. Immunofluorescence staining

BOs from all groups were inoculated into tissue culture plates, fixed with 4% paraformaldehyde (in PBS, pH 7.4) at room temperature for 15 min, and washed three times with PBS. Then, 0.1% Triton X-100 in PBS was added, and the mixture was incubated at room temperature for 15 min. Subsequently, 3% bovine serum albumin (BSA) in PBS was added, and the mixture was incubated for 60 min. The samples were then incubated with anti-vascular endothelial growth factor receptor (VEGFR; 1:150; ab2349, Abcam, United Kingdom), anti-vascular endothelial growth factor (VEGF; 1:200; ab1316, Abcam), or anti-HIF-1α (1:100; ab51608, Abcam). All samples were incubated overnight at 4 °C in a humidified chamber. After four washes with PBS containing 0.1% Tween-20 (PBST), the samples were incubated with secondary antibodies (1:400; ab150078 or ab150113, Abcam) at room temperature in the dark for 1 h. Cells were stained with 1 μg/mL 4',6-diamidino-2-phenylindole (DAPI) in PBS for 5 min, then mounted with Dako Fluorescent Mounting Medium (Agilent, USA). Images were acquired using a Zeiss LSM 800 laser scanning confocal microscope (Carl Zeiss, Germany). Three non-overlapping fields of view were randomly selected from each sample, and the average fluorescence intensity was quantified using ImageJ.

2.9. Cell proliferation assay

The dynamic changes in cell viability and proliferation within the BOs at different culture time points were evaluated using a Cell Counting Kit-8 (CCK-8) assay (CK04, Dojindo, Japan). Briefly, BOs cultured for 1, 7, or 14 days were collected and transferred into 96-well plates. Subsequently, 100 μL of fresh culture medium mixed with 10 μL of CCK-8 reagent was added to each well. After incubation at 37 °C in the dark for 2 h, the absorbance of the supernatant was measured at 450 nm using a microplate reader (Multiskan GO, Thermo Fisher Scientific, USA).

2.10. Alkaline phosphatase activity analysis

To clarify the dose–effect relationship and determine the optimal effective concentration of EVs for functional exertion, a concentration gradient experiment was performed. hFOB1.19 cells were seeded at a density of 5×10^4 cells per well in six-well plates. Following 24 h of adherence, cells were diluted to varying concentrations (10^3, 10^4, 10^5, 10^6, 10^7, and 10^8 cells/mL). After co-culture, cells were lysed, and the intracellular alkaline phosphatase (ALP) activity was quantified using the SensoLyte pNPP Alkaline Phosphatase Assay Kit (Anaspec, USA) according to the manufacturer's instructions. The processed well plate was placed in a microplate reader to determine the optical density (OD) value, and the ALP concentration was calculated from the standard curve. The specific ALP activity (U/mg protein) was subsequently normalized to the total cellular protein concentration determined by the bicinchoninic acid (BCA) assay.

2.11. Isolation and identification of extracellular vesicles

2.11.1. Isolation of extracellular vesicles from cell supernatants

Extracellular vesicles were isolated from cells through a multi-step centrifugation procedure. Specifically, for

the 2D-cultured BMSC control group (2DEV), third-passage BMSCs were seeded in T75 flasks (Corning, USA) to 80% confluence and subsequently cultured in the aforementioned osteogenic induction medium. Based on established protocols, the conditioned medium from these 2D cultures was collected after four days of continuous osteogenic induction. For the 3D BO groups, conditioned medium was collected at corresponding time points (1, 7, and 14 days; hence termed BOEV-1d, BOEV-7d, and BOEV-14d, respectively). All centrifugal processes in this study were carried out using fixed-angle rotors. After four days of culture, conditioned medium was collected, centrifuged at 300×g for 10 min, then at 1,000×g for 30 min at 4 °C to remove dead cells and cell debris. The supernatant was then collected for subsequent processing. The supernatant was centrifuged at 2,000×g for 10 min and 10,000×g for 30 min at 4 °C to remove larger microvesicles. Then, the supernatant was subjected to ultracentrifugation at 100,000×g for 70 min at 4 °C using a fixed-angle rotor (CP100NX, Hitachi, Japan). The resulting supernatant was collected and recorded as the "non-vesicular nanoparticle" fraction.[27] The EV pellet was thoroughly washed with pre-chilled Hank's balanced salt solution (HBSS) and subsequently ultracentrifuged again at 100,000×g for 70 min at 4 °C to yield the final EV preparations.

2.11.2. Proteomic sequencing and analysis of bone organoid-derived extracellular vesicles

To elucidate the specific protein cargo that mediates BOEV functions, label-free quantitative proteomic analysis was performed. Briefly, total proteins were extracted from BOEVs cultured for 1, 7, and 14 days (BOEV-1d, BOEV-7d, and BOEV-14d, respectively) using radioimmunoprecipitation assay (RIPA) lysis buffer (P0013B, Beyotime, China). Following protein reduction, alkylation, and trypsin digestion, the resulting peptides were desalted and analyzed via liquid chromatography–tandem mass spectrometry (LC–MS/MS) on an Orbitrap mass spectrometer (Thermo Fisher Scientific). The raw mass spectrometry data were searched against the UniProt rat reference database. Differentially expressed proteins (DEPs) were identified using a stringent threshold of fold change > 1.5 and p-value < 0.05. Functional clustering, GO, and KEGG pathway enrichment analyses were subsequently performed on the identified DEPs to comprehensively evaluate the enriched biological functions and signaling pathways targeted by BOEVs.

2.11.3. Bicinchoninic acid analysis

A 0.5 mg/mL protein standard solution was prepared. Based on the number of samples, an appropriate amount of BCA working solution was prepared by thoroughly mixing 50 volumes of BCA Reagent A (Thermo Fisher Scientific) with 1 volume of BCA Reagent B (50:1 ratio). To construct a standard curve, 0, 1, 2, 4, 8, 12, 16, and 20 μL of the standard solution were added to the corresponding wells of the 96-well plate. Each well was filled to a total volume of 20 μL using the standard dilution buffer, ultimately leading to standard concentrations of 0, 0.025, 0.05, 0.1, 0.2, 0.3, 0.4, and 0.5 mg/ml, respectively. A 10 μL volume of each sample was added to the wells of a 96-well plate, and standard dilution buffer was added to adjust the total volume to 20 μL. Subsequently, 200 μL of BCA working solution was added to each well, and the plate was incubated at 37 °C for 20–30 min. The absorbance was measured at 562 nm using an enzyme-linked immunosorbent assay (ELISA) reader (Synergy H1, BioTek, USA). Protein concentrations were calculated based on the standard curve and the volume of sample used.

2.11.4. Nanoparticle tracking analysis

Nanoparticle tracking analysis (NTA) was performed using the ZetaView PMX 110 instrument (Particle Metrix, Germany) and its accompanying software (ZetaView 8.02.28). Each group of EVs was diluted to a moderate level with non-particulate PBS before loading into the sample cell. Particle size distribution and concentrations were measured at 405 nm. Particle size was ultimately quantified, and the data were recorded.

2.11.5. Transmission electron microscopy

The morphology of EVs dispersed in solution was analyzed using transmission electron microscopy (TEM). Briefly, 10 μL of the EV suspension was deposited onto the center of a Parafilm membrane. A copper grid (Zhongjing Scientific Instruments, China) was inverted over the sample and incubated for 10 min to allow EV adsorption. The grid was then transferred onto a 10 μL drop of 2% phosphotungstic acid (Yuanye Bio-Technology, China) for negative staining and incubated for 5 min. Excess staining solution was removed from the edges of the grid using a strip of filter paper, and the grid was subsequently dried under an incandescent lamp positioned 15 cm away. The formulation was imaged using a Hitachi H-7650 transmission electron microscope at 80 kV.

2.11.6. PKH67 fluorescent labeling of extracellular vesicles

Extracellular vesicles were labeled with PKH67 dye (Sigma-Aldrich) according to the kit instructions. Then, 6 μL of dye was mixed with 1 mL buffer to prepare a working solution, which was slowly added to the EV solution. After incubation at room temperature for 30 min, the staining was completed. PKH67-labeled EVs were collected by centrifugation at 4 °C for 70 min at 100,000×g. After internalizing EVs in HUVECs, the labeled cells also showed fluorescent staining.

2.11.7. Extracellular vesicle internalization and uptake efficiency assay

To quantify EV uptake efficiency and cellular internalization dynamics, EVs from each group were labeled with PKH67. HUVECs and hFOB1.19 cells were seeded in 12-well plates containing glass coverslips at a density of 5×10^4 cells/well. After 24 h of adherence, cells were co-cultured with PKH67-labeled EVs at a standardized concentration (1×10^6 particles/mL). At 12 h, 24 h, and 48 h post-incubation, cells were rigorously washed with pre-chilled PBS to remove uninternalized EVs, fixed with 4% paraformaldehyde for 15 min, and stained with DAPI for 5 min. The coverslips were mounted, and images were acquired using a Zeiss LSM 800 laser scanning confocal microscope. The uptake efficiency was evaluated by quantifying the mean fluorescence intensity of PKH67 using ImageJ.

2.12. Enzyme-linked immunosorbent assay

According to the manufacturer's instructions, species-specific ELISA kits (ELK Biotechnology, China) were used to quantify osteogenic markers (ALP [ELK5657], bone morphogenetic protein 2 [BMP-2; ELK1405], transforming growth factor beta 1 [TGF-β1; ELK2311]), angiogenic factors (VEGF [ELK2320], HIF-1α [ELK1604]), and syndecan-4 (SDC4; ELK6005) in EVs. The specific steps were as follows: EVs isolated from each group were resuspended in pre-chilled PBS and lysed using RIPA lysis buffer supplemented with 1% protease inhibitor cocktail (P8340, Sigma-Aldrich) and 1% phosphatase inhibitor cocktail (P5726, Sigma-Aldrich). The lysis reaction was conducted on ice for 30 min with gentle vortexing every 5 min, followed by centrifugation at 12,000×g for 15 min at 4 °C to collect the supernatant. Prior to ELISA, the protein concentration of each EV lysate was normalized to 50 μg/mL using the BCA protein assay kit (23225, Thermo Fisher Scientific) to ensure equal EV input. Soluble protein carryover was excluded by two rounds of washing with pre-chilled PBS during the EV isolation process (100,000×g for 70 min at 4 °C each time). After centrifugation (3,000×g, 15 min), the samples from each treatment group were placed into precoated antibody microplates for incubation. Subsequently, the corresponding detection antibodies were added to continue incubation. The absorbance was measured at 450 nm using a microplate reader, and the concentration was determined based on the standard curve.

2.13. Western blot

Total protein was extracted from cells and exosomes and separated on 10%–15% sodium dodecyl sulfate (SDS)–polyacrylamide gels according to the molecular weight of the target proteins. Proteins were transferred onto polyvinylidene fluoride (PVDF) membranes (IPVH00010, Merck Millipore, Germany) and blocked with 5% skim milk for 1 h. Membranes were incubated overnight at 4 °C with primary antibodies against: CD63 (1:1,500; ab213090, Abcam), CD81 (1:2,000; MA532333, Invitrogen), ALG-2-interacting protein X (ALIX; 1:1,500; ab186429, Abcam), tissue-nonspecific alkaline phosphatase (TNAP; 1:1,500; BS9818M, Emelcabioscience, China), annexin V (1:1,500; #8555, Cell Signaling Technology, USA), calnexin (1:1,500; ab22595, Abcam), SMAD family member 1 (SMAD1; 1:1,500; 051459, Merck Millipore), RUNX family transcription factor 2 (RUNX2; 1:1,500; ab76956, Abcam), TGF-β1 (1:1,500; ab179695, Abcam), BCL2-associated X protein (BAX; 1:1,000; ab182733, Abcam), B-cell lymphoma 2 (BCL-2; 1:1,000; ab194583, Abcam), cleaved caspase-3 (1:1,000; ab214430, Abcam), glyceraldehyde-3-phosphate dehydrogenase (GAPDH; 1:1,500; ab263962, Abcam), and β-actin(1:1,500; ab8227, Abcam). Secondary antibodies (goat anti-mouse IgG, 1:3,000; ab205719, Abcam; and goat anti-rabbit IgG, 1:3,000; ab205718, Abcam) were applied. Protein bands were visualized using enhanced chemiluminescence (ECL) reagents (P0018S, Beyotime) and imaged using a ChemiDoc MP system (Bio-Rad, USA).

2.14. Co-culture of bone organoid-derived extracellular vesicles with human umbilical vein endothelial cells and tube formation assay

Human umbilical vein endothelial cells were starved in serum-free endothelial cell culture medium for 6 h. Cells were digested with 0.25% trypsin–EDTA, centrifuged at 300×g for 5 min, and resuspended to a density of 3×10^5 cells/mL. Matrigel (10 mg/mL; Corning) was thawed on ice, and 50 μL was added to each pre-chilled 96-well plate well, then incubated at 37 °C for 1 h to solidify. Subsequently, 50 μL of cell suspension (1.5×10^4 cells/well) mixed with BOEVs (BOEV-1d, BOEV-7d, BOEV-14d), 2DEV (negative control), or pre-chilled PBS (control group) was added. Prior to the co-culture, each freshly isolated batch of EVs was immediately subjected to NTA to precisely determine the initial particle concentration. Based on these fresh measurements, the EV suspensions were subsequently diluted and standardized to a final concentration of 1×10^6 particles/mL in each treatment group, ensuring uniform vesicle input. After 24 h of co-culturing, the cultures were inoculated into the matrix gel. Plates were incubated at 37 °C with 5% CO_2 for 6–8 h. Images were captured via inverted microscopy. ImageJ was used to quantify the total length of the vascular network and the number of nodes to evaluate the angiogenic effect of each EV group. Furthermore, to validate the specific downstream effects of *Hif1a* knockdown, HUVECs were treated in parallel with BOEV-HIF-1α-KD-7d under identical conditions, followed by RT-qPCR analysis to evaluate the expression of angiogenic markers.

2.15. Co-culture of bone organoid-derived extracellular vesicles with hFOB1.19 cells

Human osteoblast cell line hFOB1.19 was seeded into six-well plates at a density of 5×10^4 cells per well and cultured in DMEM supplemented with 10% exosome-free fetal bovine serum and 1% penicillin–streptomycin (10,000 U/mL) at 37 °C in a humidified incubator with 5% CO_2. After 24 h of adherence, the culture medium was replaced with fresh complete medium containing BOEVs (BOEV-1d, BOEV-7d, or BOEV-14d) or 2DEV. Similarly, prior to addition, the particle concentration of each freshly isolated EV batch was quantified via NTA, and the suspensions were standardized to a final concentration of 1×10^6 particles/mL to ensure consistent vesicle input across all groups. The positive control group was treated with osteogenic induction medium (containing 10 mM β-glycerophosphate, 50 μM trisodium salt-2-phosphate-*L*-ascorbic acid, and 100 nM dexamethasone) at the same volume as EV treatments. The control group received an equal volume of pre-chilled PBS without EVs. All groups were cultured for 21 days, with the corresponding medium (containing EVs or osteogenic induction components) replaced every three days. At the end of the culture period, alizarin red S staining and RT-qPCR analysis were performed to evaluate osteogenic differentiation. Similarly, to functionally confirm the role of the HIF-1α axis, hFOB1.19 cells were treated with BOEV-HIF-1α-KD-7d under the corresponding experimental conditions, and the expression of osteogenesis-related genes was assessed by RT-qPCR.

2.16. Alizarin red S staining

Each group of cells was washed three times with DPBS. The 1 d, 7 d, and 14 d groups were fixed with 4% paraformaldehyde for 30 min. After washing with deionized water, the samples were incubated at room temperature with a 1% alizarin red S solution (pH 4.2; Cyagen, China) for 30 min. All sample groups were observed and photographed using a macro-camera (D7500, Nikon, Japan). The brief procedure is as follows: after gently washing the microplate, the stained precipitate was incubated with 10% hexadecyl pyridinium chloride (Sigma) for 30 min. Absorbance was measured at 620 nm using a Synergy H1 microplate reader.

2.17. Statistical analysis

Sample sizes (n) represent independent biological replicates. The sample sizes for each experiment were determined based on preliminary results, expected effect sizes, and established conventions for specific in vitro assays to ensure adequate statistical power. Assays with high reproducibility (e.g., RT-qPCR, Western blotting, and alizarin red S staining) were performed with $n = 3$. Assays involving higher intrinsic biological variability, such as tube formation networks, utilized $n = 5$. For EV yield and cytokine profiling, extended biological replicates ($n = 6–10$) were used to account for inter-batch variations in isolation. SPSS 23.0 (IBM Corp, USA) was used to conduct the statistical analysis. The statistics are presented as mean ± standard deviation (SD). For comparisons between two groups, Student's *t*-test was used. For comparisons among three or more groups, one-way ANOVA was employed, followed by Tukey's post-hoc test for multiple comparisons to evaluate statistical significance between specific group pairs. Categorical variables are expressed in counts and percentages, and comparisons were made through a Chi-squared test. The correlations were obtained using the Spearman correlation method. A p-value < 0.05 was considered statistically significant.

3. Results

3.1. Construction of bone organoids

We isolated BMSCs from Sprague–Dawley rat femurs to construct BOs. Flow cytometry analysis confirmed the phenotypic identity of isolated BMSCs, showing high expression of positive surface markers (CD73, CD90) and negligible expression of negative markers (CD34, CD45) (Figure S1). In 3D culture plates, cells aggregated and grew into multicellular spheroids. BO-1d, BO-7d, and BO-14d represent different culture days. All three BO groups were treated with osteogenic induction medium (Figure 1A). The growth status of BOs on a 3D culture plate was observed under a microscope at 0, 12, and 24 h post-seeding. At 0 h, the seeded cells were suspended in the 3D culture plate. At 12 h, the cells began to aggregate, forming small cell clusters. By 24 h, the structure of early BOs was preliminarily established (Figure 1B). After one day of 3D culture, the BOs were transferred to conventional plates. BO-1d spheroids were numerous and small. The size of BO-7d and BO-14d spheroids increased over time, yet their numbers decreased due to unintentional aspiration during media change, as well as possible cell death and spheroid disintegration (Figure 1C). Quantification of osteogenesis-related genes in BOs was performed. Relative mRNA expression levels of *Runx2*, *Sp7*, *Col1a1*, and *Ocn* in BO-1d, BO-7d, and BO-14d are presented in Figure 1D. *Runx2* and *Ocn* showed significant upregulation in BO-7d compared with BO-1d, with a further increase in BO-14d. *Sp7* and *Col1a1* peaked in BO-7d but decreased in BO-14d. SEM imaging showed that early-stage BOs (BO-1d) had relatively smooth surfaces. However, for BO-7d and BO-14d, the surface appeared to have shriveled apoptotic cells and extracellular matrix deposition (Figure 1E). Spheroid size distribution analysis reported an average size of 115.58 ± 25.36 μm for BO-1d. The average size increased to 148.62 ± 35.72 μm for BO-7d and further to 203.71 ± 45.30 μm for BO-14d, showing a general trend of enlargement over time (Figure 1F). Quantification of spheroid numbers

revealed a decrease from BO-1d to BO-14d (Figure 1G). To investigate whether this reduction was functionally linked to altered cell viability, we evaluated dynamic changes in cell proliferation and apoptosis in BOs at different culture time points. The CCK-8 assay showed a progressive and significant decrease in cell proliferation over time (Figure 1H). Concurrently, Western blot analysis of key apoptosis-related proteins revealed that the expression of the anti-apoptotic marker BCL-2 decreased over time, whereas the pro-apoptotic markers BAX and cleaved caspase-3 were markedly upregulated at later culture stages (Figure 1I). These functional findings provide evidence that the reduction in spheroid number is indeed closely linked to diminished cell proliferation and increased apoptosis. The above results indicate that we successfully constructed BOs using primary BMSCs and 3D culture plates, and as the spheroids gradually enlarged under osteogenic induction, they experienced survival restrictions potentially driven by central hypoxia as the organoids matured. The successful construction of BOs provides an experimental basis for further study of spheroid function at different developmental stages.

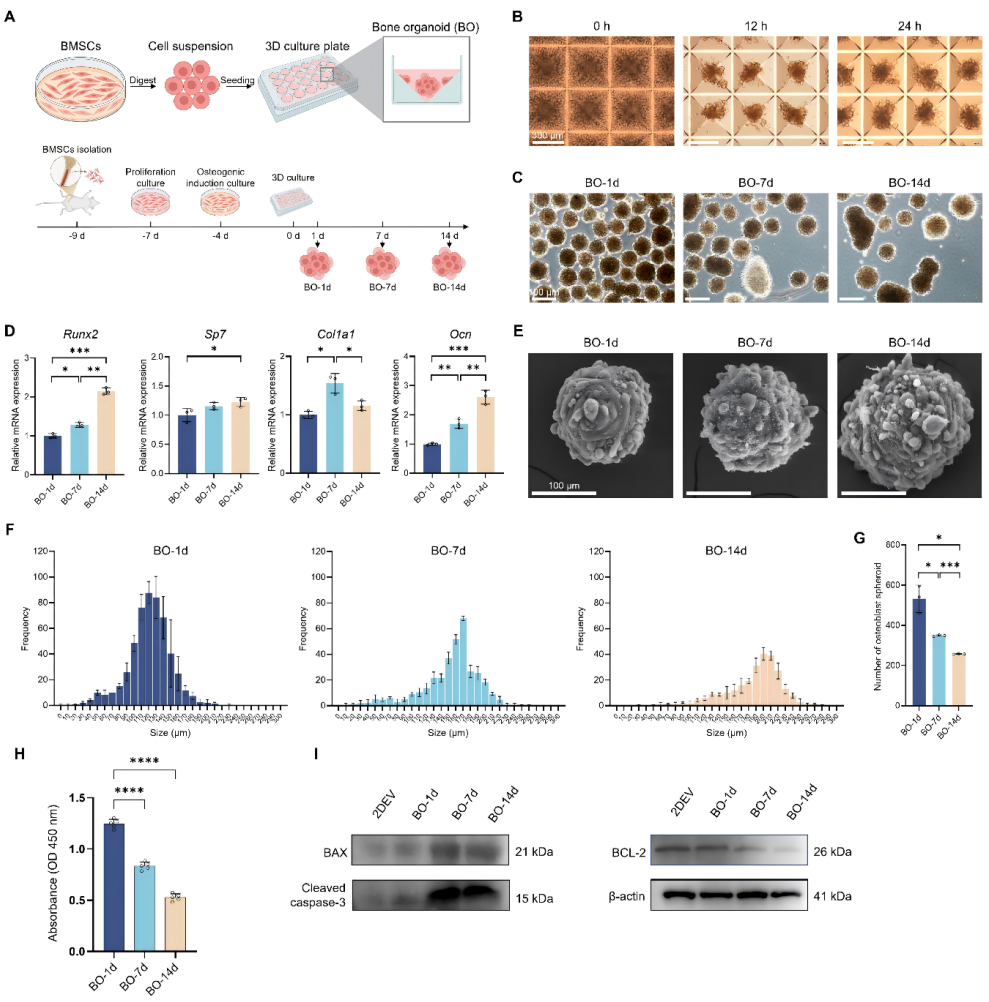

Figure 1. Construction of bone organoids (BOs). (A) Schematic of BO construction and groups. Created in BioRender.com. Li, S. et al. (2026) https://app.biorender.com/illustrations/686b1d4b300c9062cb3fda96?slideId=d6087077-bc71-4b1c-804a-db26b0b1d651. (B) Bright-field images of bone marrow mesenchymal stem cells (BMSCs) in 3D culture plates at 0, 12, and 24 h. Scale bars: 300 μm; magnification: 40×. (C) Bright-field images of free-floating BOs. Scale bars: 100 μm; magnification: 100×. (D) Quantitative polymerase chain reaction (qPCR) analysis of osteogenesis-related messenger RNA (mRNA) expression in BOs $n = 3$). (E) Scanning electron microscopy (SEM) images of BOs. Scale bars: 100 μm; magnification: 800×. (F) Size measurement and frequency distribution of BOs based on SEM images ($n = 3$). (G) Quantification of osteoblast spheroids based on SEM images ($n = 3$). (H) Cell-Counting Kit (CCK)-8 assay evaluating the cell viability of BOs at different culture durations ($n = 6$). (I) Western blotting analysis of apoptosis-related proteins (BCL2-associated X protein [BAX], cleaved caspase-3, and B-cell lymphoma 2 [BCL-2]) in BOs ($n = 3$).
Notes: $^{*}p < 0.05$, $^{**}p < 0.01$, $^{***}p < 0.001$.
Abbreviation: OD: Optical density.

3.2. Progressive expression of osteogenic and angiogenic factors in bone organoids

By performing mRNA sequencing on 2D-cultured BMSCs, BO-1d, BO-7d, and BO-14d, we generated a heatmap to analyze the DEGs. A total of 270 genes showed more than two-fold differential expression (Figure 2A; the detailed gene list and corresponding statistical metrics are provided in Table S1). Through GO enrichment analysis of the DEGs (applying a *p*.adj cutoff of <0.05), in biological processes (BP), we found that in addition to a significant correlation with the osteoblast differentiation pathway (*p*.adj = 2.5e−10), there was also a highly significant difference in response to hypoxia (*p*.adj = 7.5e−10, GeneRatio = 0.038), especially in the BO-7d and BO-14d groups. In the cellular component (CC) analysis, cell–cell junction and focal adhesion were highly enriched; moreover, there was a significant correlation with transport vesicle and transport vesicle membrane. In the molecular function (MF) analysis, functions such as cadherin binding and GTPase binding were highly enriched. These analyses indicate that these DEGs may not only promote osteogenesis but also be associated with angiogenesis and with BOEVs (Figure 2B). The KEGG analysis results (*p*.adj < 0.05) showed that pathways such as regulation of actin cytoskeleton and signaling pathways regulating pluripotency of stem cells were significantly enriched, and the VEGF signaling pathway also showed a significant correlation, suggesting a role in promoting angiogenesis (Figure 2C). Based on mRNA sequencing results, we performed experimental verification of BOs; immunofluorescence staining showed that as the osteogenic induction time increased, the distribution and intensity of VEGFR fluorescence signals in cells gradually increased (Figure 2D). To directly confirm the underlying regulatory mediators, we further performed immunofluorescence assessment for VEGF and its upstream transcriptional regulator, HIF-1α. As shown in Figure 2F, the images clearly demonstrate robust and distinct spatial expression of both HIF-1α and VEGF within the BOs. Quantitative analysis of the mean fluorescence intensity (Figure 2G) further corroborated these visual observations, revealing a significant upregulation of both HIF-1α and VEGF proteins at the later stages of 3D culture (BO-7d and BO-14d) compared to the early stage (BO-1d). This direct protein-level evidence perfectly aligns with the upregulation of VEGFR, reinforcing the establishment of the HIF-1α–VEGF regulatory axis within the hypoxic microenvironment of the BOs. qPCR was performed to identify key genes in 2D-cultured BMSCs, BO-1d, BO-7d, and BO-14d. Compared with 2D-cultured BMSCs, the expression levels of Alp, Hif1a, and Rab27a in BOs gradually increased over time and were consistent with mRNA sequencing results. This indicates their involvement in osteogenesis, angiogenesis, and EV release (Figure 2E). It is worth noting that Hif1a and Rab27a showed no significant difference ($p > 0.05$) in mRNA levels between the BO-7d and BO-14d groups. The former indicates that the hypoxic environment and related angiogenesis pathways in BOs were upregulated in the middle and late stages of 3D culture, whereas the latter indicates an increase in BOEV secretion levels during the same stages.

These results identified the DEGs between 2D-cultured BMSCs and 3D-cultured BO cells. In-depth studies of these DEGs showed that they may be involved in osteogenic differentiation, angiogenesis promotion, and EV release facilitation. These results also suggest that BOEVs with different culture times may not only promote bone differentiation but also stimulate angiogenesis.

3.3. Characterization of bone organoid-derived extracellular vesicles and their enrichment with osteogenic and angiogenic factors

We isolated EVs from the culture supernatant of 2D-cultured BMSCs and BOs, termed 2DEV, BOEV-1d, BOEV-7d, and BOEV-14d (Figure 3A). EV concentrations were estimated based on protein concentration. The BOEV-7d (85.11 ± 10.95 μg/mL) and BOEV-14d (92.33 ± 14.05 μg/mL) groups showed no significant difference ($p > 0.05$) but were both significantly higher than BOEV-1d (60.36 ± 6.49 μg/mL). Compared to 2DEV (27.08 ± 3.31 μg/mL), BOEV groups had 2–3 times higher EV protein concentrations (Figure 3B). NTA confirmed that all EV groups had a particle size peak around 100 nm. Consistently, particle concentration trends showed BOEV-7d and BOEV-14d had the highest vesicle counts, followed by BOEV-1d, with 2DEV being the lowest (Figure 3C). Furthermore, to assess the purity of the isolated EVs according to standardized characterization metrics, we calculated the particle-to-protein ratio by dividing the particle concentration (measured via NTA) by the total protein concentration (measured via BCA assay) for each group (Figure 3D). The analysis revealed that the 2DEV group exhibited a significantly higher particle-to-protein ratio than all BOEV groups, which stabilized at approximately 7×10^5 particles/μg. Rather than indicating low vesicular purity, this lower numerical ratio in the 3D-cultured groups reflects the profound enrichment of extracellular matrix proteins, specific matrix vesicles, and pro-angiogenic/osteogenic factors actively secreted by the 3D organoids into the vesicle corona, significantly elevating the total protein denominator. To further characterize BOEVs and rigorously evaluate their purity, we performed Western blotting to assess the expression of classic EV marker proteins, along with a negative control marker. The results showed that CD63, CD81, and ALIX were all positively expressed in all groups. Concurrently, calnexin, an endoplasmic reticulum contaminant marker, was completely absent across all groups, confirming

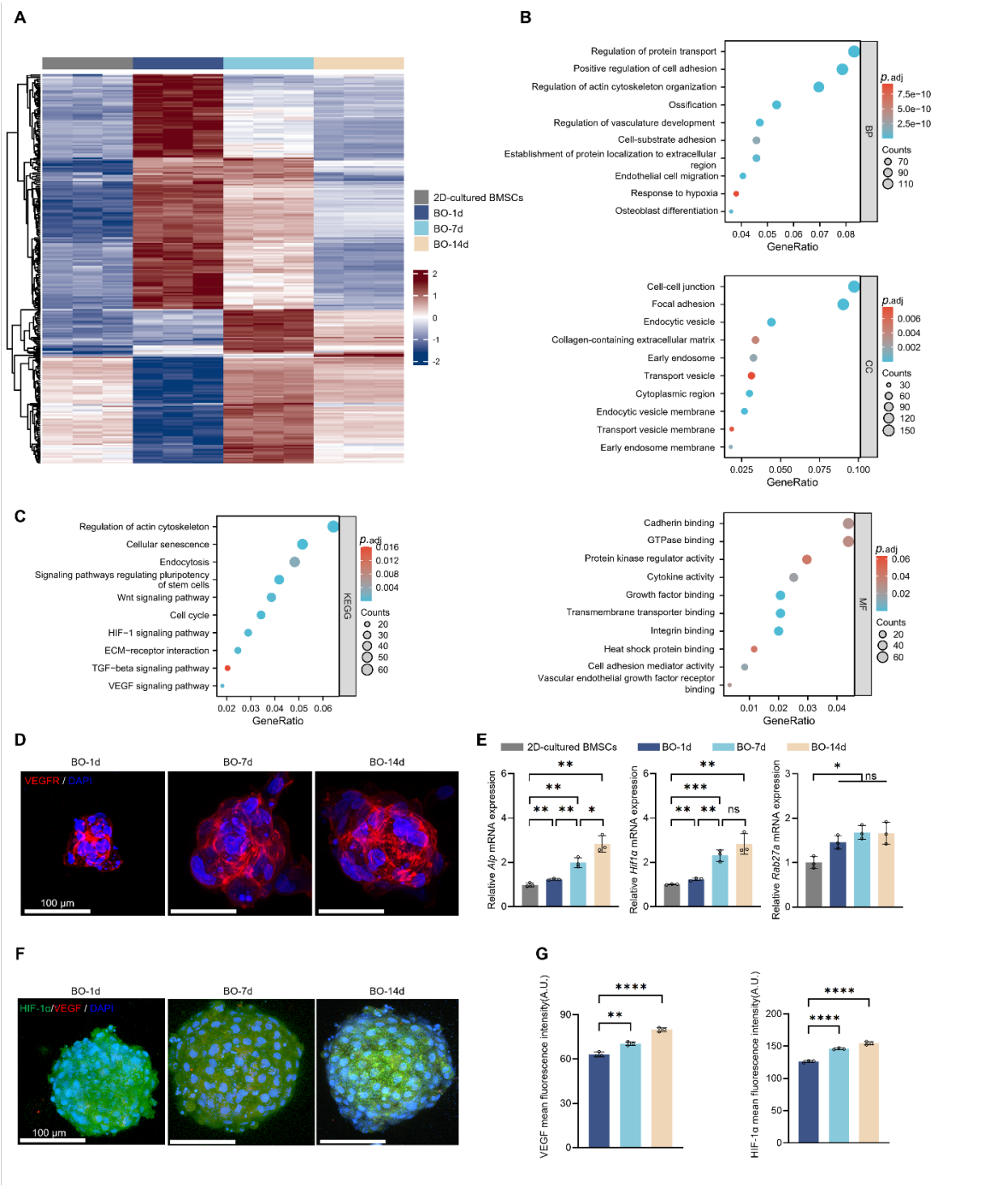

Figure 2. Messenger RNA (mRNA) sequencing and validation of bone organoids (BOs). (A) Heat map of two-fold differentially expressed genes (DEGs) (n = 3). (B) Gene Ontology (GO) functional enrichment analysis of DEGs (n = 3). (C) Kyoto Encyclopedia of Genes and Genomes (KEGG) pathway enrichment analysis of DEGs (n = 3). (D) Immunofluorescence staining of VEGFR. Scale bars: 100 μm; magnification: 200×. (E) Quantitative analysis of *Alp*, *Hif1a*, and *Rab27a* mRNA expression (n = 3). (F) Immunofluorescence staining of hypoxia-inducible factor-1α (HIF-1α; green) and vascular endothelial growth factor (VEGF; red) in BOs at different culture durations. Scale bar: 100 μm; magnification: 200×. (G) Quantitative analysis of the mean fluorescence intensity of VEGF and HIF-1α (n = 3).

Notes: $^{*}p < 0.05$, $^{**}p < 0.01$, $^{***}p < 0.001$, ns: $p > 0.05$.

Abbreviations: BMSC: Bone marrow mesenchymal stem cell; DAPI: 4′,6-diamidino-2-phenylindole; ECM: Extracellular matrix; TGF: Transforming growth factor.

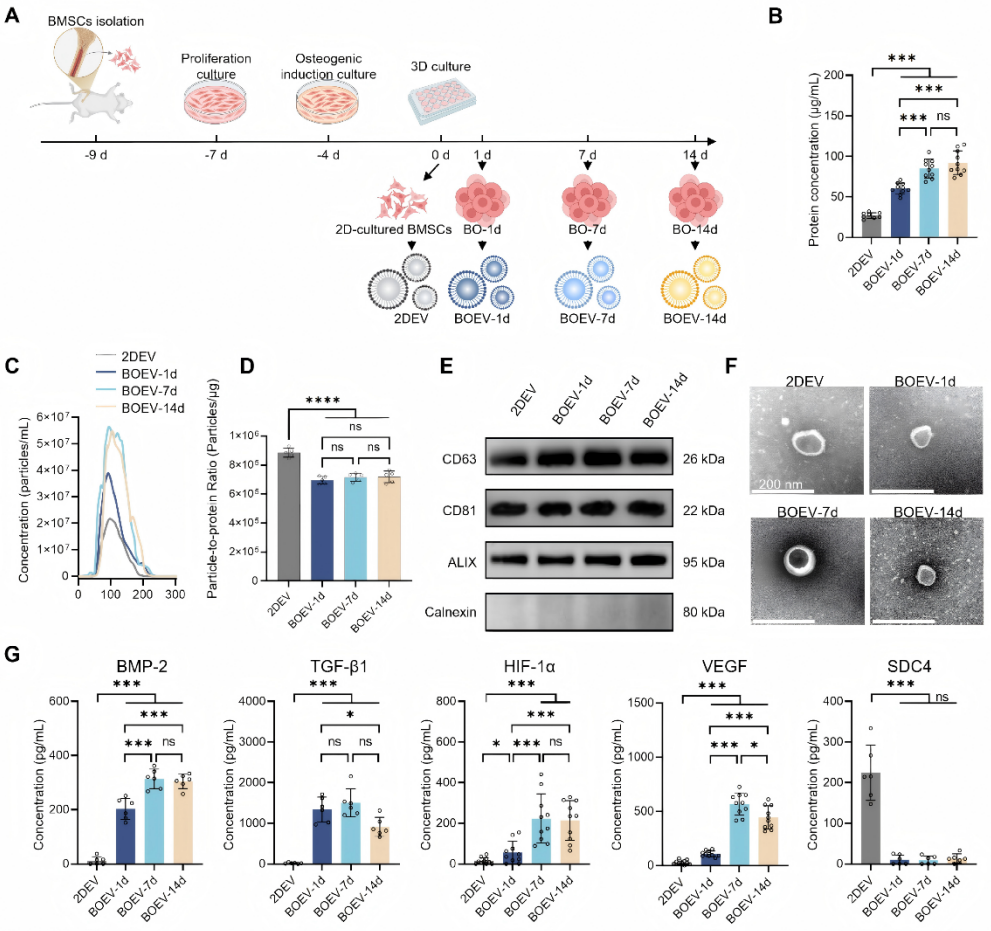

Figure 3. Extracellular vesicle (EV) characterization and growth factor assessment. (A) Schematic diagram of preconditioning for EVs in each group. Created in BioRender.com. Li, S. et al. (2026) https://app.biorender.com/illustrations/686b1d4b300c9062cb3fda96?slideId=d6087077-bc71-4b1c-804a-db26b0b1d651. (B) Bicinchoninic acid (BCA) analysis of EV protein concentration (n = 10). (C) Nanoparticle tracking analysis (NTA) of EV size and concentration (n = 3). (D) Quantitative analysis of the particle-to-protein ratio (particles/μg) across groups (n = 5). (E) Western blotting of BOEV markers (n = 3): CD63, CD81, ALG-2-interacting protein X (ALIX), calnexin. (F) Transmission electron microscopy (TEM) of EV morphology. Scale bars: 200 nm; magnification: 30,000×. (G) Enzyme-linked immunosorbent assay (ELISA) quantification of bone morphogenetic protein 2 (BMP-2), transforming growth factor beta 1 (TGF-β1), hypoxia-inducible factor-1α (HIF-1α), vascular endothelial growth factor (VEGF), and syndecan-4 (SDC4) concentrations in EVs (n = 7).
Notes: *$p < 0.05$, **$p < 0.01$, ***$p < 0.001$, ns: $p > 0.05$.

that the isolated EVs were free from cellular organelle contamination and met strict molecular characterization standards (Figure 3E). Furthermore, to explore the presence of matrix vesicles associated with BOEVs, we conducted additional Western blotting analysis, confirming the expression of matrix vesicle-specific positive markers, TNAP and annexin V, in BOEV-1d, BOEV-7d, and BOEV-14d (Figure S2). TEM revealed that EVs in all groups ranged in size from 50 to 200 nm, with typical features of spherical, membrane-like vesicles (Figure 3F). These results indicate that we successfully isolated EVs derived from 2D-cultured BMSCs and BOs. Further analysis, guided by prior mRNA sequencing results, involved ELISA to quantify protein levels of osteogenic and angiogenic factors (Figure 3G). In the BOEV-7d group, BMP-2 (314.00 ± 33.09 pg/mL), TGF-β1 (1,500.67 ± 315.94 pg/mL), HIF-1α (223.10 ± 114.51 pg/mL), and VEGF (566.8 ± 96.78 pg/mL) were the highest among all groups. The BOEV-14d group showed no significant differences in BMP-2, TGF-β1, and HIF-1α levels compared to BOEV-7d ($p > 0.05$), but its VEGF level (422.8 ± 100.62 pg/mL) was significantly lower. Meanwhile, BOEV-1d had significantly lower levels of BMP-2, HIF-1α, and VEGF than BOEV-7d and BOEV-14d, except for TGF-β1. Notably, the levels of these factors in 2DEV were significantly lower than those in the BOEV groups ($p < 0.001$). An exception was SDC4, which exhibited a high protein level of 224.33 ± 62.03 pg/mL in 2DEV; this protein is closely associated with cell adhesion and maintenance of

morphology and typically exhibits lower expression levels in 3D cultures.

These findings indicate that BOs effectively secrete EVs that are enriched in osteogenic and angiogenic factors. This implies that BOEVs, especially BOEV-7d, may promote osteogenic differentiation and angiogenesis. Furthermore, to establish the optimal dosage for subsequent functional evaluations, we investigated the dose–response relationship between EV concentration and ALP activity in hFOB1.19 cells (Figure S3). Across all groups, ALP activity exhibited a characteristic sigmoidal dose–response pattern across the tested EV concentration range (10^3 to 10^8 particles/mL). Notably, the pro-osteogenic effect reached a functional plateau at a concentration of 1×10^6 particles/mL, beyond which further increases in dosage yielded no significant additional enhancement in ALP activity. Based on this dose-effect relationship, 1×10^6 particles/mL was selected as the standardized working concentration for all subsequent in vitro co-culture assays to ensure both maximal efficacy and experimental consistency.

3.4. Proteomic profiling of key angiogenic and osteogenic functional cargos in bone organoid-derived extracellular vesicles

While mRNA sequencing of the parent organoids provided critical transcriptomic insights, we also performed LC–MS/MS-based proteomics directly on the BOEVs (BOEV-1d, BOEV-7d, and BOEV-14d) to identify the specific functional protein targets mediating their biological effects. Consistent with our mRNA transcriptomic data, proteomic profiling revealed distinct protein cargo clusters that dynamically shifted with culture duration (Figure 4). Compared to BOEV-1d, BOEV-7d and BOEV-14d exhibited significant enrichment of DEPs primarily associated with extracellular matrix organization, vascular endothelial cell migration, and bone mineralization. GO and KEGG enrichment analyses of these DEPs further confirmed the pronounced activation of the HIF-1α, VEGF, and TGF-β/BMP signaling pathways. Furthermore, the high-throughput proteomic data precisely aligned with our ELISA and Western blotting target validation assays (Figure 3E and 3G), explicitly corroborating the robust encapsulation of core functional factors within the vesicles. These proteomic validations bridge the mechanistic gap between the parent organoids' transcriptomic alterations and the functional capacities of the vesicles.

3.5. Equivalent internalization of bone organoid-derived extracellular vesicles across different culture durations

To clarify the basis of functional differences across EV groups and ensure dose–response consistency, we evaluated the cellular uptake efficiency of PKH67-labeled EVs in both HUVECs and hFOB1.19 cells using confocal microscopy. Following co-culture with standardized initial EV particle inputs (1×10^6 particles/mL), confocal imaging of HUVECs demonstrated that PKH67-labeled EVs (green fluorescence) successfully entered the cells and primarily accumulated in the perinuclear region (Figure 5A). The fluorescence intensity exhibited a clear time-dependent dynamic across 12, 24, and 48 h; however, at each time point, the visual distribution and intensity of green fluorescence appeared virtually indistinguishable across all groups. Subsequent quantitative analysis of relative mean fluorescence intensity in HUVECs corroborated this observation, revealing no significant differences ($p > 0.05$) in uptake efficiency across all groups at any time point (Figure 5B).

Similarly, in the hFOB1.19 osteoblast cell line, confocal fluorescence images confirmed an identical pattern of time-dependent EV internalization (Figure 5C). The corresponding mean fluorescence intensity quantification for hFOB1.19 cells further demonstrated that uptake efficiencies were completely equivalent across all EV groups at 12, 24, and 48 h, with no statistical significance observed (Figure 5D). Together, these equivalent cellular internalization profiles confirm that standardizing the EV dosage leads to consistent intracellular accumulation. Consequently, this demonstrates that the superior downstream angiogenic and osteogenic functional outcomes observed in the BOEV-7d group are driven by qualitative differences in specific molecular payloads rather than by enhanced rates of cellular entry.

3.6. BOEV-7d promotes angiogenesis in human umbilical vein endothelial cells

We co-cultured BOEVs with HUVECs to evaluate their potential pro-angiogenic capacity. After internalizing fluorescence-labeled BOEVs, HUVECs exhibited green fluorescence and displayed a vascular-like tube formation tendency in Matrigel. The BOEV groups exhibited a more extensive and tightly connected vascular-like network than the control and 2DEV groups, with the BOEV-7d group demonstrating the most robust tube formation (Figure 6A). Further quantitative analysis revealed that the BOEV groups exhibited significantly higher total vascular length and node counts than both the control and 2DEV groups, consistent with the aforementioned angiogenic fluorescence imaging results. The BOEV-7d group reached the highest values for total vascular length (5,182.60 ± 958.11 μm) and node count (307.40 ± 44.42), indicating that BOEVs promote vasculoid formation, with the most pronounced effect observed at seven days post-treatment (Figure 6B). Pro-angiogenic efficacy did not increase monotonically with extended BOEV culture duration; although both BOEV-1d and BOEV-14d exhibited comparable effects, their potency was significantly inferior to that of BOEV-7d.

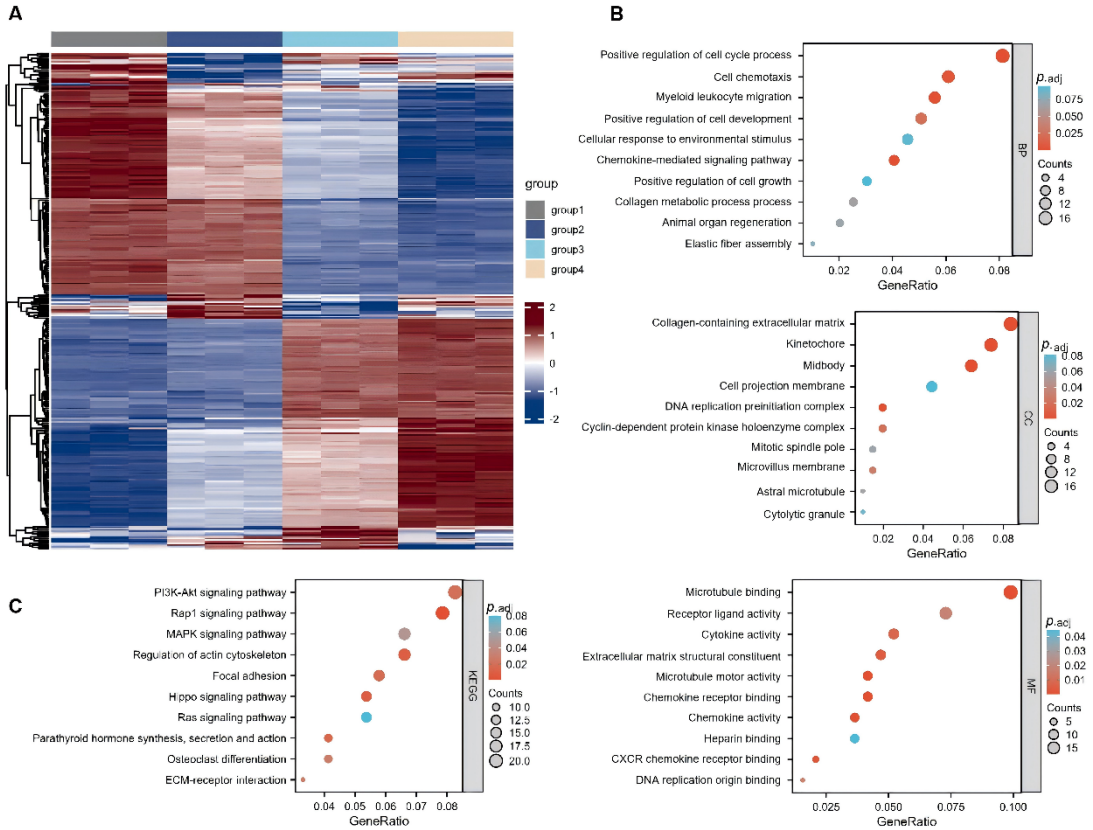

Figure 4. Proteomic profiling of bone organoid-derived extracellular vesicles (BOEVs) across different culture durations. (A) Heatmap showing hierarchical clustering of differentially expressed proteins (DEPs; $|\log_2$ fold change$| > 1.5$) across groups. (B) Gene Ontology (GO) enrichment analysis of the DEPs, categorized into biological process (BP), cellular component (CC), and molecular function (MF). (C) Kyoto Encyclopedia of Genes and Genomes (KEGG) pathway enrichment analysis of the DEPs. In the bubble charts (B and C), the bubble size indicates the gene protein count, and the color gradient represents the adjusted p-value (*p*.adj).
Abbreviations: Akt: Protein kinase B; BMSC: Bone marrow mesenchymal stem cell; CXCR: C–X–C chemokine receptor; ECM: Extracellular matrix; MAPK: Mitogen-activated protein kinase; PI3K: Phosphoinositide 3-kinase.

Relative mRNA expression levels of the angiogenesis genes *Vegf*, *Ccn2*, and *Fn* were analyzed. *Vegf* in the BOEV-7d group was significantly higher than in other groups. No significant differences in *Ccn2* levels were observed across BOEV groups, whereas *Fn* expression was highest in the BOEV-14d group. All three mRNAs positively regulate HUVEC adhesion, migration, and tube formation (Figure 6C). To validate the causal role of HIF-1α in BOEV-mediated angiogenesis and osteogenesis, we supplemented *Hif1a*-knockdown experiments in BMSCs prior to BO construction, with knockdown efficiency confirmed using qPCR (Figure S4A). SEM images of *Hif1a*-knockdown BOs were captured (Figure S4B). The cells agglomerated into organoids, but the spreading growth state of the cells was significantly lower than that of BO-7d. Subsequent analysis of BOEV-HIF-1α-KD-7d revealed significantly reduced HIF-1α and VEGF protein levels compared to BOEV-7d (Figure S4C). To confirm that this impact is functional, we evaluated HUVECs treated with the *Hif1a*-knockdown EVs. Our qPCR analysis demonstrated that the expression of key angiogenic markers (*Vegf*, *Ccn2*, and *Fn*) was significantly attenuated in the BOEV-HIF-1α-KD-7d group compared to the BOEV-7d group (Figure S4D). This further supports the HIF-1α–VEGF regulatory axis proposed in our study.

These results demonstrate that BOEVs possess pro-angiogenic properties, corroborating the upregulation of angiogenic factors observed in our prior mRNA sequencing data.

3.7. Osteogenic differentiation of osteoblasts by bone organoid-derived extracellular vesicles

To explore the effects of BOEVs on osteogenic differentiation, we co-cultured them with the hFOB1.19 osteoblast line and analyzed them using alizarin red S staining. The positive control group showed the greatest ability to promote

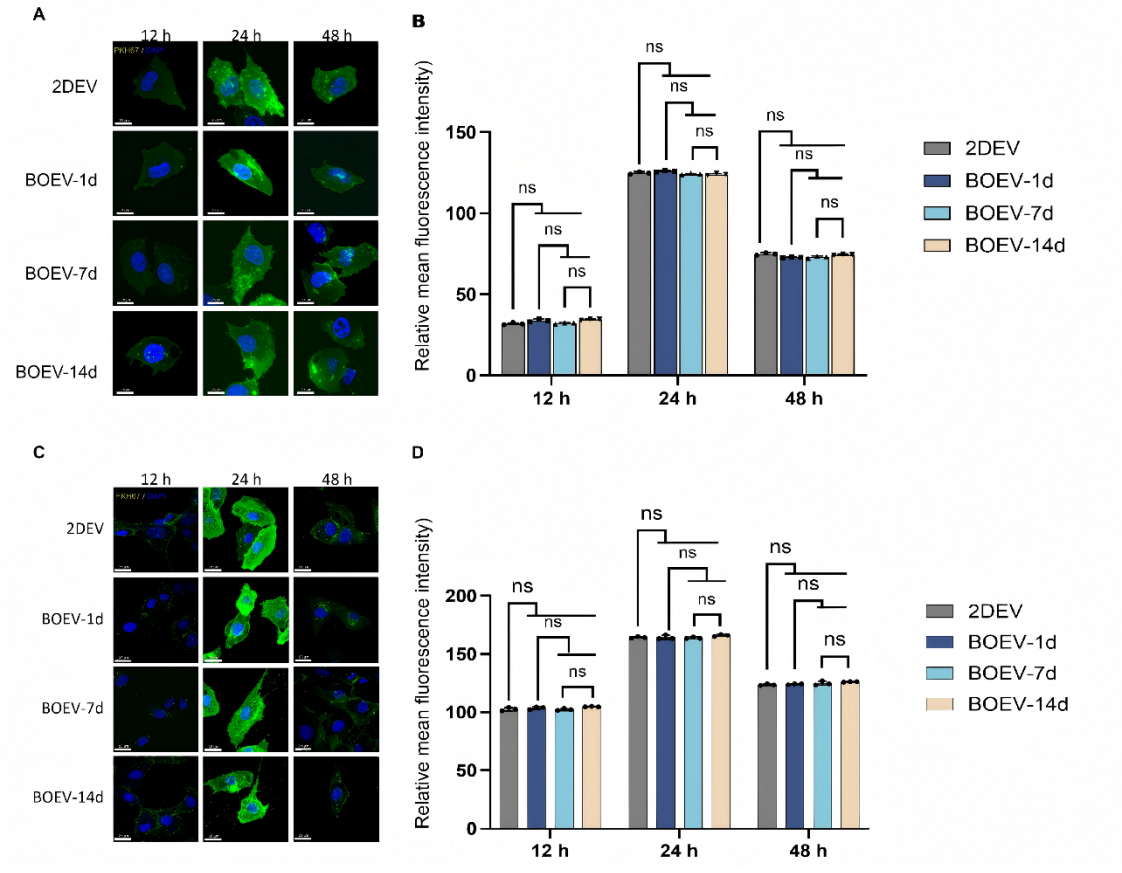

Figure 5. Equivalent internalization efficiency of bone organoid-derived extracellular vesicles (BOEVs) across different culture durations. (A) Representative confocal fluorescence images showing the cellular uptake of PKH67-labeled extracellular vesicles (EVs; green) by human umbilical vein endothelial cells (HUVECs) at 12, 24, and 48 h. Nuclei were stained with 4′ ,6-diamidino-2-phenylindole (DAPI; blue). (B) Quantitative analysis of the relative mean fluorescence intensity of PKH67 in HUVECs (n = 3). (C) Representative confocal fluorescence images showing the cellular uptake of PKH67-labeled EVs (green) by hFOB1.19 cells at 12, 24, and 48 h. Nuclei were stained with DAPI (blue). (D) Quantitative analysis of the relative mean fluorescence intensity of PKH67 in hFOB1.19 cells (n = 3).
Notes: Scale bars: 25 μm; magnification: 60×. ns: $p > 0.05$.

bone differentiation compared with the untreated control and 2DEV groups. The staining intensity of mineralized nodules in the BOEV groups was substantially enhanced, and the degree of red mineralization increased gradually with increasing treatment time (Figure 7A). The statistical analysis of OD values for mineralized nodules showed that the staining depth of BOEV-14d was significantly greater than that of the other two BOEV groups (Figure 7B). The mRNA expression levels of osteogenic differentiation-related genes *Runx2*, *Sp7*, *Col1a1*, and *Ocn* were assessed using RT-qPCR. The results showed that the positive control group expressed all the genes tested. Compared with the untreated control group, the 2DEV and all BOEV groups showed significantly upregulated expression of *Runx2*, *Sp7*, *Col1a1*, and *Ocn*. Additionally, the expression of all these genes in the BOEV groups was higher than that of the 2DEV group. However, it is worth noting that for *Sp7*, there was no significant difference between the BOEV-7d group, BOEV-14d group, and the positive control group. For *Col1a1*, its expression in the BOEV-14d group was lower than that of the BOEV-7d group, but not statistically significant (Figure 7C). Western blotting analysis further confirmed that BOEVs significantly upregulated BMP-2, RUNX2, and TGF-β1 in hFOB1.19 cells (Figure 7D). Together with alizarin red S staining results, these findings comprehensively verified the mineralization-promoting capacity of BOEVs.

In addition, to rule out the effects of non-vesicular nanoparticles that may be present in EVs on osteogenic differentiation, we quantified ALP concentration and enzymatic activity in all BOEV groups and in non-vesicular nanoparticles using ELISA and a colorimetric assay. Both ALP concentration and activity were significantly higher in the BOEV groups than in non-vesicular nanoparticles

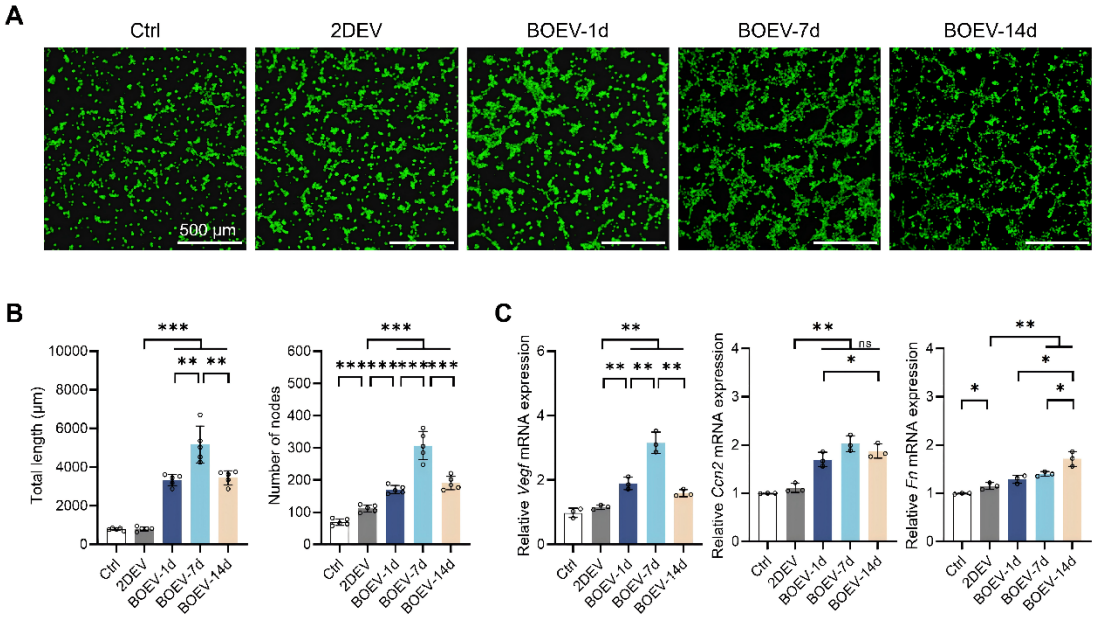

Figure 6. Bone organoid-derived extracellular vesicles (BOEVs) promote angiogenesis in human umbilical vein endothelial cells. (A) Fluorescence imaging analysis of vascular-like structures induced by PKH67-labeled extracellular vesicles (EVs). Scale bars: 500 μm; magnification: 4×. (B) Quantitative analysis of total length and number of nodes of vascular-like structures (n = 5). (C) Relative messenger RNA (mRNA) expression levels of *Vegf*, *Ccn2*, and *Fn* (n = 3).
Notes: *$p < 0.05$, **$p < 0.01$, ***$p < 0.001$, ns: $p > 0.05$.

($p < 0.0001$), and showed a time-dependent increase in the BOEV groups, confirming that BOEVs are enriched with functionally active ALP (Figure S5A) and verifying the morphological characteristics of non-vesicular nanoparticles via TEM (Figure S5B). To further validate the specificity of BOEV-mediated angiogenic effects, we quantified VEGF secretion. We found that non-vesicular nanoparticles induced minimal VEGF release, whereas BOEVs significantly promoted VEGF secretion, indicating that the observed angiogenic effects are primarily driven by EVs rather than non-vesicular nanoparticles (Figure S5C). Consequently, these data demonstrate that non-vesicular components exhibit weaker, but still present, bioactivity in these specific biochemical assays compared to intact BOEVs. To further substantiate the mechanistic role of HIF-1α in downstream osteogenesis, we analyzed hFOB1.19 cells exposed to EVs from the *Hif1a*-knockdown organoids. The BOEV-7d-induced upregulation of osteogenic markers (*Runx2*, *Sp7*, *Col1a1*, and Ocn) was markedly reversed following *Hif1a* knockdown (Figure S4E), directly linking the molecular alteration to the cellular phenotype.

These results suggest that BOEVs exhibit properties that promote osteogenic differentiation, although they do not reach the level of the positive control group.

4. Discussion

Bone defect repair is a crucial problem that urgently needs to be addressed in orthopedic clinical practice. Developing highly efficient and low-cost treatment strategies holds significant clinical value. Relevant research has confirmed that BO has demonstrated promising efficacy in bone defect repair.[28] However, this technology has limitations, such as a complex construction process and high preparation costs, which hinder its clinical translation and popularization.[1,29] At present, research on BOEVs has not received sufficient attention. EVs have been shown to have a therapeutic effect on bone defects.[30-32] Against this research backdrop, BOEVs are theoretically capable not only of regulating bone regeneration but also of serving as biological markers reflecting the growth and development status of BO. However, to date, no systematic research in this regard has been reported.

We constructed BOs using rat primary BMSCs and an osteogenic-induction 3D culture plate. We verified the specific surface biomarkers of isolated BMSCs by flow cytometry, confirming their phenotypic identity and purity for use in this study. Under osteogenic induction, the BOs gradually increased in size and expressed genes related to osteogenesis. In a recent study by Chen *et al.*[33], primary BMSCs were extracted from the iliac bone marrow of six-month-old New Zealand white rabbits. The differentiation potential of these BMSCs was evaluated through osteogenic and chondrogenic induction. Subsequently, cartilage organoids were constructed using a 3D organoid mold.

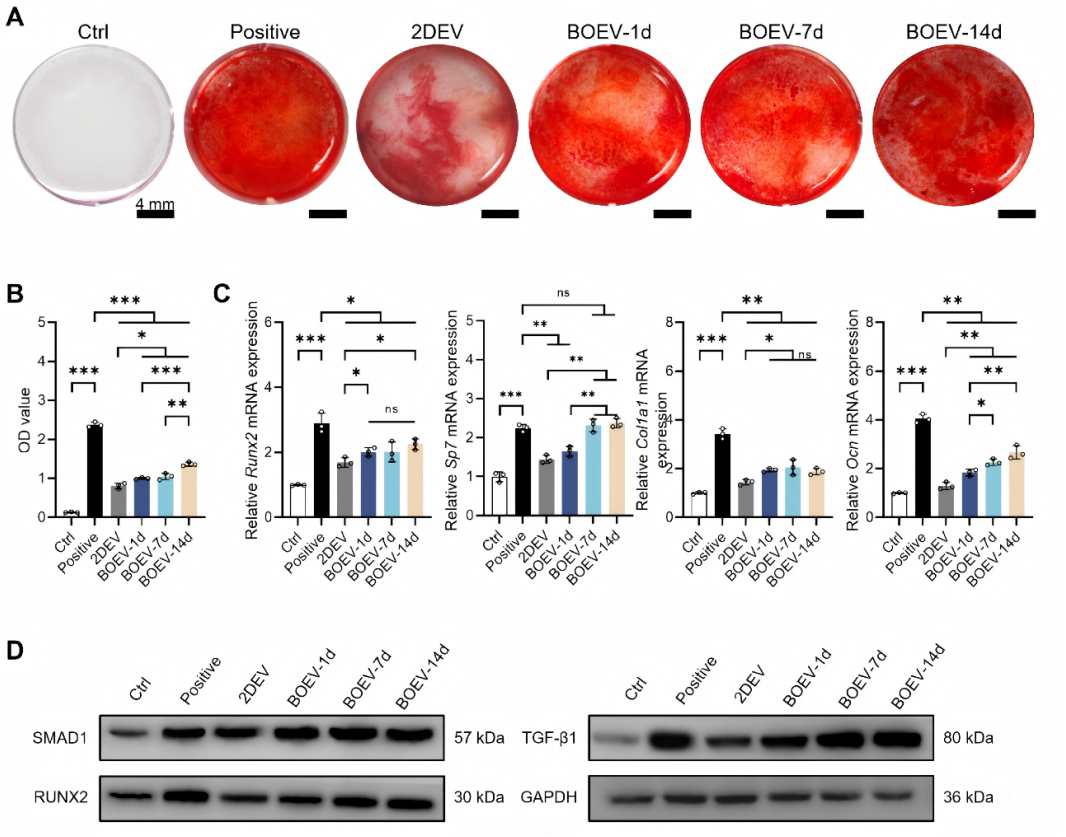

Figure 7. Bone organoid-derived extracellular vesicles (BOEVs) promote osteoblast differentiation. (A) Alizarin red S staining in hFOB1.19 cells at day 21. Scale bars: 4 mm; magnification: 1×. (B) Quantitative analysis of optical density (OD) values in alizarin red R staining ($n = 3$). (C) Messenger RNA (mRNA) expression levels of *Runx2*, *Sp7*, *Col1a1*, and *Ocn* in hFOB1.19 cells at day 21 ($n = 3$). (D) Western blotting of the osteogenic-related molecules in hFOB1.19 cells at day 21 ($n = 3$).
Notes: $^{*}p < 0.05$, $^{**}p < 0.01$, $^{***}p < 0.001$, ns: $p > 0.05$.
Abbreviations: GAPDH: Glyceraldehyde-3-phosphate dehydrogenase; RUNX2: RUNX family transcription factor; SMAD1: SMAD family member 1; TGF-β1: Transforming growth factor beta 1.

Drawing on the successful experience in constructing and evaluating BOs or cartilage organoids, the organoids we constructed can be classified as BOs. We grouped the BOs by culture time. As the BOs grew larger, they encountered a common problem in organoids: central hypoxia. To assess the effects of this phenomenon on organoid survival, we included cell proliferation and apoptosis assays. Our functional data successfully captured this dynamic process: as culture duration and organoid volume increased, the BOs exhibited a continuous decline in cell proliferation capacity, coupled with a prominent upregulation of pro-apoptotic markers (BAX and cleaved caspase-3) and a simultaneous downregulation of the anti-apoptotic marker BCL-2. These results confirm our hypothesis that the macroscopic reduction in BO spheroid number over time is driven by central hypoxia-induced cellular apoptosis and diminished viability. In previous studies on organoids, it has been clearly demonstrated that hypoxia in the central region of organoids can lead to functional changes and cellular necrosis.[34] A recent systematic review and meta-analysis encompassing 91 articles indicates that EVs can effectively promote the regeneration of bone defects.[30] However, to date, no research has been conducted on the functions of BOEVs. Given the potentially close relationship between the overall function of organoids and EVs, as well as the significant impact of central hypoxia on organoid function, we reasonably speculate that BOEV function would also change accordingly. We performed RNA-sequencing on BMSCs cultured in 2D and BOs cultured in 3D, and carried out differential gene expression analysis, GO enrichment analysis, and KEGG enrichment analysis. The results showed that BOs are highly associated with osteoblast differentiation pathways, vesicle transport, and hypoxic responses.

The gradual increase in ALP concentration and enzymatic activity in BOEVs, coupled with the stable expression of canonical EV-positive markers and the absence of the negative control marker calnexin, solidifies

the identity of these vesicles as functional mineralization inducers rather than passive cellular debris. This finding directly addresses the concern regarding insufficient EV characterization, as it explicitly rules out endoplasmic reticulum or intracellular contamination. It demonstrates that our isolated BOEVs possess high purity and the archetypal biophysical properties of EVs, while also carrying enzymatically active ALP, a key functional mediator of matrix mineralization in bone tissue engineering. Our study found that, compared with EVs cultured in 2D, the yield of BOEVs was increased, and their morphology was consistent with the structural characteristics of EVs.[35] Further ELISA showed that BMP-2, TGF-β1, HIF-1α, and VEGF were present in BOEVs, and their protein concentrations were higher than those of EVs cultured in 2D. These findings indicate that BOs can effectively secrete EVs rich in osteogenic and angiogenic factors. Furthermore, as observed in our EV quantification data, normalizing EV concentrations to a standardized particle number (1×10^6 particles/mL) still resulted in varying total protein concentrations across groups, indicating inconsistent protein loading per individual vesicle. By calculating the protein-to-particle ratio, we observed higher protein masses per vesicle in the BOEV groups, particularly at later culture stages. This discrepancy can primarily be attributed to two factors. First, the distinct culture conditions—specifically the shift from 2D monolayers to 3D biomimetic structures with emerging hypoxic cores—profoundly alter cellular metabolic states and cargo-sorting mechanisms, prompting cells to actively package higher levels of functional proteins (such as angiogenic and osteogenic factors) into vesicles. Second, in the highly active secretory microenvironment of 3D BOs, abundant extracellular matrix proteins are released into the culture medium. These ambient proteins can dynamically adsorb onto the lipid bilayer of the secreted EVs, forming a "protein corona" on the vesicle surface. The formation of this protein corona increases the measured protein mass per quantified particle. Consequently, our calculated particle-to-protein ratio was approximately 10^5 particles/μg. Although this numerical ratio is notably lower than the traditional threshold for ultra-high-purity EVs (typically > 10^9 particles/μg), it accurately reflects the specific biological complexity of the 3D organoid system rather than a limitation of the isolation technique. Additionally, the biomimetic mineralization process inherent to BOs enriches BOEVs with specialized matrix vesicles containing a high density of functional proteins. Furthermore, our reliance on standard ultracentrifugation inevitably co-purifies some non-vesicular proteins, which further increases the total protein denominator. This phenomenon highlights that the functional characteristics of BOEVs are derived not only from their altered intra-vesicular cargo but also potentially from the bioactive protein corona acquired within the specialized organoid microenvironment. Importantly, relying solely on mRNA sequencing of parent organoids limits the ability to fully define the functional mediators interacting with target cells. To overcome this and address the direct mechanism of action, we supplemented this with comprehensive proteomic sequencing of BOEVs at different culture durations. The resulting proteomic landscape corroborated our prior transcriptomic findings, unveiling a highly specialized enrichment of pro-angiogenic and pro-osteogenic protein cargos in BOEV-7d and BOEV-14d. The identification of these key functional targets through LC–MS/MS—alongside our Western blot and ELISA validations—provides direct, objective evidence that BOEVs do not merely passively reflect the parent organoids' physiological status, but actively package and deliver specific regenerative protein networks to successfully orchestrate downstream vascularized osteogenesis. It suggests that BOEVs may promote osteogenic differentiation and angiogenesis. Our functional validation assays demonstrated that the pro-osteogenic and pro-angiogenic bioactivities observed in the present study are predominantly mediated by BOEVs, with residual non-vesicular nanoparticles exerting significantly weaker effects in these assays. The research by Hao *et al.*[36] indicated that exosomes derived from Schwann cells encapsulated in a neural tissue-engineering hydrogel (SC-Exo) can significantly enhance bone regeneration by promoting *in vivo* innervation, immunomodulation, angiogenesis, and osteogenesis. In addition, Wang *et al.*[37] suggested that lactylation of HIF-1α promotes upregulation of *Vegfa*, thereby stimulating angiogenesis in endothelial cells. To verify the angiogenic potential of BOEVs, we co-cultured them with HUVECs and found that BOEV groups formed a more extensive and tightly connected vascular-like network. Similarly, in Hao *et al.*'s[36] study, to explore the direct effects of hydrogel-encapsulated Schwann cell exosomes (SC-Exo/hydrogel) on angiogenic capacity, they co-cultured SC-Exo/hydrogel with HUVECs. The SC-Exo/hydrogel group had more vascular sprouts. Quantitative analysis indicated significant advantages in the number of vascular nodes and segments, as well as the total length of the vascular network. The formation of new blood vessels is crucial for the survival of bone cells and the integration of implants with bone tissue. Insufficient angiogenesis leads to inadequate nutrient supply, cell death, and reduced bone formation at the defect site.[38] A large number of studies have shown that, in bone tissue engineering, constructing a novel scaffold platform that simultaneously induces osteogenesis and angiogenesis has become a cutting-edge treatment strategy for bone defects.[39] Related research has indicated that EVs can mediate biomineralization.[40] During bone mineralization, EVs play a crucial role in transporting biomineralization precursors and mineralized collagen fibers.[41] In addition, matrix

vesicles are a special subtype of exosomes that share overlapping biosynthetic pathways with EVs, including exosome-like polycystic body-derived and exosome-like plasma membrane budding pathways, and promote bone mineralization by concentrating calcium phosphate ions and by expressing key mineralization regulatory factors, such as TNAP and annexin V.[42] It is worth noting that BOEVs may encapsulate functional matrix vesicles, as evidenced by the enrichment of matrix vesicle-related proteins, such as TNAP and annexin V, in BOEVs and by the greater intensity in alizarin red S staining. This is consistent with the role of matrix vesicles in providing nucleation sites for hydroxyapatite formation during bone matrix mineralization. Apart from participating in mitochondrial autophagy-mediated mineral transport, EVs can also detach from the plasma membrane and regulate calcium and phosphate ion reactions in the extracellular matrix through various mechanisms.[40] Based on the above-mentioned research, we co-cultured BOEVs with hFOB1.19 cells. The results showed that the staining intensity of mineralized nodules in the BOEV groups was significantly enhanced. Moreover, as treatment time increased, the degree of red-colored mineralization gradually increased, suggesting that BOEVs promote osteogenic differentiation. We confirmed through Western blotting that BOEVs significantly upregulated BMP-2, RUNX2, and TGF-β1 in hFOB1.19 cells. These data, combined with alizarin red S staining results, demonstrate that BOEVs promote osteoblast mineralization. We speculate that BOEVs may promote osteogenic differentiation by upregulating VEGF via increased HIF-1α expression, thereby facilitating angiogenesis. In evaluating the angiogenic potential of BOs, it is worth noting that VEGF is a secreted paracrine factor continuously released into the culture medium. This characteristic inherently makes it more challenging to capture robust, localized fluorescence signals in 3D whole-organoid preparations compared to membrane-bound receptors, such as VEGFR. Nonetheless, our supplemented immunofluorescence analyses confirmed the presence and expression of both VEGF and HIF-1α within the BOs. This spatial distribution not only confirms the presence of a hypoxic core but also substantiates the HIF-1α–VEGF regulatory axis driving the subsequent BOEV-mediated vascular regeneration. To further consolidate the causal link between HIF-1α in BOEVs and the observed pro-angiogenic/osteogenic effects, we supplemented *Hif1a* knockdown experiments in BMSCs prior to BO construction, with knockdown efficiency validated by qPCR. SEM images of *Hif1a*-knockdown BOs were captured, and subsequent detection confirmed that BOEV-HIF-1α-KD-7d exhibited significantly reduced HIF-1α and VEGF protein levels compared to BOEV-7d, strongly suggesting the involvement of the HIF-1α–VEGF regulatory axis underlying BOEV-mediated bone and vascular regeneration. Crucially, our downstream functional assays demonstrated that the robust pro-angiogenic and pro-osteogenic responses typically induced by BOEV-7d in target cells were significantly reversed when utilizing EVs from the *Hif1a*-knockdown organoids. This transforms the molecular observation into a fully integrated mechanistic study. These supplementary data reinforce the notion that HIF-1α in BOEVs is not merely a correlative factor but a key mediator driving downstream angiogenic and osteogenic pathways, strengthening the mechanistic rigor of our findings. Furthermore, defining the optimal effective concentration is critical for maximizing therapeutic efficacy while maintaining experimental rigor. Using our newly developed concentration gradient evaluation, we established a clear dose–response relationship, demonstrating that the pro-osteogenic functional exertion (indicated by ALP activity) of BOEVs saturates at 1×10^6 particles/mL. All EV inputs for functional experiments in this study were standardized by quantifying vesicle numbers using NTA, ensuring consistent EV doses across groups and eliminating interference from dose differences in experimental results. Furthermore, our quantitative assessment of EV internalization via confocal microscopy revealed equivalent uptake efficiencies across all EV groups in both HUVECs and hFOB1.19 cells. This finding provides critical support for our dose–response consistency, suggesting that standardizing extracellular particle input results in comparable intracellular vesicle accumulation. Consequently, it implies that the significant functional discrepancies observed—particularly the enhanced pro-angiogenic and pro-osteogenic capacities of BOEV-7d—are unlikely to be primarily driven by differential rates of vesicle cellular entry. Instead, these therapeutic advantages may largely be attributed to qualitative differences in their molecular payloads. We speculate that the specialized regenerative protein cargos (e.g., HIF-1α, VEGF, and BMP-2), which are preferentially enriched within the vesicles during the specific 3D biomimetic culture window, play a predominant role in orchestrating these enhanced downstream cellular responses. It is worth noting that the size, quantity, and donor cell status of bone-like organs change dynamically over culture time. Subsequent studies will further establish the correlation between the number and vitality of organoid cells and BOEV production and protein composition, optimize normalization strategies, and provide a more rigorous experimental basis for related functional mechanism research.

Our research demonstrates that BOEV is a key factor that promotes angiogenesis and osteogenic differentiation *in vitro*, and it provides a novel BOEV-based research direction for exploring bone defect repair strategies. To fully appreciate the therapeutic potential of BOEVs, it is

imperative to contextualize them against conventional stem cell-derived EVs and other organoid-derived EVs. Compared to traditional 2D mesenchymal stem cell-derived EVs, BOEVs exhibit pronounced regenerative advantages. As systematically summarized in recent perspectives by Liu *et al.*[24], the 3D biomimetic architecture of organoids restores complex cell–matrix and cell–cell crosstalk, closely mimicking the native in vivo niche. Our data demonstrate that this 3D spatial organization—coupled with the intrinsic central hypoxia—drives a dramatic enrichment of specific angiogenic and osteogenic cargos (e.g., HIF-1α, VEGF, and BMP-2) in BOEVs, endowing them with superior dual-lineage regenerative efficacy over 2DEVs. Furthermore, while EVs derived from other organoid types (such as brain and intestinal organoids) play crucial roles in their respective microenvironments[43], BOEVs possess a highly tissue-specific repertoire. Specifically, the biomimetic mineralization process inherent to BOs[44] enriches BOEVs with specialized matrix vesicles that express TNAP and annexin V. This equips BOEVs to nucleate hydroxyapatite and orchestrate bone matrix mineralization, a distinct advantage in orthopedic applications compared to generic organoid-derived EVs. Despite these biological advantages, using 3D organoid culture for EV production offers both unique advantages and formidable translational limitations. On the upside, 3D culture significantly enhances EV yield per cell and produces a cargo profile with greater physiological fidelity.[24] However, as highlighted in the recent consensus and perspective articles[12,44], the scalable production of BOEVs faces significant bottlenecks. The high cost of 3D matrices, batch-to-batch structural heterogeneity, and the lack of standardized large-scale isolation protocols limit their immediate clinical translation. Additionally, while moderate central hypoxia stimulates beneficial pro-angiogenic EV packaging, uncontrolled organoid overgrowth can lead to severe central necrosis, potentially deteriorating EV quality and triggering inflammatory responses.[12] Therefore, developing standardized, automated, and dynamically perfused biofabrication techniques to reliably harness the therapeutic potential of BOEVs remains a critical frontier for future research. This study has some limitations that need to be acknowledged. First, no *in vivo* animal experiments were conducted in this study; this will be further improved in subsequent research. Second, this study has not yet elucidated the protein composition changes of bone-like organs and their EVs at different culture times. Third, regarding the EV internalization assays, we utilized the non-covalent lipophilic dye PKH67. While stringent washing and ultracentrifugation steps were rigorously performed to remove unbound dye, the inherent limitations of lipophilic dyes—such as potential free dye aggregation and non-specific membrane transfer—cannot be eliminated without advanced co-localization analysis or brightfield overlays. It is important to note that the primary purpose of PKH67 staining in this study was to broadly visualize the macroscopic tube-like network morphology of HUVECs, rather than to track the precise subcellular internalization dynamics of EVs. Therefore, while the potential presence of free dye might exert a minor impact on high-resolution fluorescence observations, it does not detract from the robust functional endpoints demonstrated in our study. Fourth, while our supplementary assessments (such as ALP activity and VEGF secretion) indicate that co-purified non-vesicular nanoparticles exhibit weaker but detectable bioactivity compared to BOEVs, we acknowledge that these specific biochemical markers do not represent a comprehensive evaluation of cellular functions. As recently demonstrated by Morales-Sanfrutos *et al.*[27], we acknowledge the inherent limitations of our ultracentrifugation isolation protocol without density gradient or size-exclusion chromatography. Ultracentrifugation cannot completely separate bona fide EVs from non-vesicular protein aggregates and nucleic acids. Therefore, we hypothesize that the robust therapeutic potential observed in this study may be driven by the synergistic action of the EV fraction (which critically includes functional matrix vesicles, as evidenced by TNAP and annexin V enrichment) and the co-isolated non-vesicular proteins. Future studies encompassing density gradient separation and detailed functional profiling of these non-vesicular fractions are required to precisely delineate the individual contributions of true EVs versus non-vesicular components within the regenerative microenvironment. This will be the core focus of our subsequent research, which aims to explore the correlation between organoid development and BOEV protein composition. Finally, a critical limitation of the current study is our reliance on rat-derived BMSCs for BO construction. While our findings establish the pro-angiogenic and pro-osteogenic efficacy of rat-derived BOEVs, species-specific discrepancies pose an inevitable challenge for direct clinical translation. As extensively highlighted in recent consensus frameworks and frontiers[12,43,44], human-derived organoids represent the future of disease modeling and regenerative medicine. Human-derived stem cells—such as patient-specific mesenchymal stem cells—enable the creation of highly biomimetic organoid platforms that faithfully recapitulate the intricate structural complexity, specific pathological environments, and unique cellular crosstalk of human skeletal tissues.[43] Importantly, human-derived BOs offer greater physiological relevance and circumvent the interspecies immunogenicity and genetic differences inherent to rodent models.[44] Consequently, whether human-derived BOEVs possess an identical HIF-1α-mediated paracrine profile capable of inducing comparable vascularized osteogenesis remains a pivotal question. Future studies must prioritize scalable biofabrication of human-derived BOs to harvest human-specific BOEVs.[26] Rigorously validating their therapeutic equivalence and

exploring their personalized regenerative potential will be an indispensable step toward advancing BOEV-based therapies from in vitro models to clinical applications in human bone defects.

5. Conclusion

In conclusion, this study successfully established BOs derived from rat BMSCs and demonstrated the potent regenerative capacities of their secreted BOEVs. As the BOs matured in 3D culture, central hypoxia naturally emerged, triggering the HIF-1α–VEGF regulatory axis and driving the active encapsulation of crucial angiogenic and osteogenic factors—including BMP-2, TGF-β1, HIF-1α, and VEGF—into the BOEVs. Notably, EVs harvested on day 7 (BOEV-7d) exhibited the most robust therapeutic potential, significantly enhancing vascular network formation in endothelial cells and accelerating matrix mineralization in osteoblasts compared to conventional 2D-cultured stem cell EVs. These findings provide compelling in vitro evidence that BOEVs exert dual functional roles in orchestrating both angiogenesis and osteogenesis. In summary, this study demonstrates the potential of BOEVs for bone defect repair, providing a preliminary experimental basis for subsequent *in vivo* animal studies.

Acknowledgments

The graphical abstract was created in BioRender. Li, S. *et al.* (2026) https://app.biorender.com/illustrations/686b1d4b300c9062cb3fda96?slideId=d6087077-bc71-4b1c-804a-db26b0b1d651.

Funding

This work was supported by the National Natural Science Foundation of China (82300018 to SL), the Guangdong Basic and Applied Basic Research Foundation (2025A1515012604 to SL), the Fujian Provincial Natural Science Foundation of China (2025J08345 to WS), the Medical Research Foundation of Putian University (2024114 to WS), the National Center for Translational Medicine (Shanghai) SHU Branch of Shanghai University (SUITM-202503 to HL), and the Youth S&T Talent Support Programme of Guangdong Provincial Association for Science and Technology (to SL).

Conflict of interest

The authors declare that there are no conflicts of interest.

Author contributions

Conceptualization: Guobing Chen, Shiyu Li, Wengang Liu, Weiwei Su
Formal analysis: Zhenning Dai, Suiqing Huang
Investigation: Wenqiang Zhou
Methodology: Jiarui Liu, Jingyuan Huang, Ruoqi Ma
Visualization: Zhenning Dai, Ding Li, Hui Lu
Writing–original draft: Zhenning Dai, Ding Li
Writing–review & editing: Shiyu Li
All authors have read and agreed to the published version of the manuscript.

Ethics approval and consent to participate

All animal experiments were conducted in accordance with the ethical guidelines for laboratory animal care and were approved by the Animal Ethics Committee of Jinan University (Approval No. JNU107391).

Consent for publication

Not applicable.

Availability of data

Data and materials are available from the corresponding authors upon reasonable request.

References

1. Hong Y, Li R, Sheng S, Zhou F, Bai L, Su J. Bone organoid construction and evolution. *J Orthop Translat*. 2025;53:260-273.

   doi: 10.1016/j.jot.2025.06.011

2. Zhang P, Qin Q, Cao X, *et al*. Hydrogel microspheres for bone regeneration through regulation of the regenerative microenvironment. *Biomater Transl*. 2024;5(3):205-235.

   doi: 10.12336/biomatertransl.2024.03.002

3. Huang J, Li A, Liang R, *et al*. Future perspectives: advances in bone/cartilage organoid technology and clinical potential. *Biomater Transl*. 2024;5(4):425-443.

   doi: 10.12336/biomatertransl.2024.04.007

4. Steijvers E, Ghei A, Xia Z. Manufacturing artificial bone allografts: a perspective. *Biomater Transl*. 2022;3(1):65-80.

   doi: 10.12336/biomatertransl.2022.01.007

5. Zhong G, Miao Y, Zhou J, *et al*. Near-infrared light-induced photothermal and immunotherapy system for lung cancer bone metastasis treatment with simultaneous bone repair. *Bioact Mater*. 2025;52:182-199.

   doi: 10.1016/j.bioactmat.2025.06.008

6. Zhao Z, Chen X, Dowbaj AM, *et al*. Organoids. *Nat Rev Methods Primers*. 2022;2:94.

   doi: 10.1038/s43586-022-00174-y

7. Wang W, Zhang T, Wang J, Wang W, Sun H. Engineering bone organoids: Recent advances and future prospects. *Organoid Res*. 2025;1(4):025330027.

   doi: 10.36922/OR025330027

8. Lancaster MA, Knoblich JA. Organogenesis in a dish: modeling development and disease using organoid

technologies. *Science*. 2014;345(6194):1247125.

doi: 10.1126/science.1247125

9. Liu H, Su J. Organoid and organoid extracellular vesicles for osteoporotic fractures therapy: Current status and future perspectives. *Interdiscip Med*. 2023;1(3):e20230011.

doi: 10.1002/inmd.20230011

10. Li A, Liang R, Sheng W, *et al.* Global research trends in bone/cartilage organoids from 2010 to 2024: A bibliometric and visualization study. *Organoid Res*. 2025;1(3):8295.

doi: 10.36922/or.8295

11. Wang J, Xia Z, Su J. Organoid research breakthroughs in 2024: A review. *Organoid Res*. 2025;1(2):025040005.

doi: 10.36922/OR025040005.

12. Wang J, Chen X, Li R, *et al.* Standardization and consensus in the development and application of bone organoids. *Theranostics*. 2025;15(2):682-706.

doi: 10.7150/thno.105840

13. Wang J, Wu Y, Li G, *et al.* Engineering Large-Scale Self-Mineralizing Bone Organoids with Bone Matrix-Inspired Hydroxyapatite Hybrid Bioinks. *Adv Mater*. 2024;36(30):e2309875.

doi: 10.1002/adma.202309875

14. Dmitriev RI, Papkovsky DB. Multi-parametric O_2 imaging in three-dimensional neural cell models with the phosphorescent probes. *Methods Mol Biol*. 2015;1254:55-71.

doi: 10.1007/978-1-4939-2152-2_5

15. Song YS, Lin RL, Montesano G, *et al.* Engineered 3D tissue models for cell-laden microfluidic channels. *Anal Bioanal Chem*. 2009;395(1):185-193.

doi: 10.1007/s00216-009-2935-1

16. Maisumu G, Willerth S, Nestor MW, *et al.* Brain organoids: building higher-order complexity and neural circuitry models. *Trends Biotechnol*. 2025;43(7):1583-1598.

doi: 10.1016/j.tibtech.2025.02.009

17. Choe MS, Kim SJ, Oh ST, *et al.* A simple method to improve the quality and yield of human pluripotent stem cell-derived cerebral organoids. *Heliyon*. 2021;7(6):e07350.

doi: 10.1016/j.heliyon.2021.e07350

18. Li A, Sasaki JI, Abe GL, Katata C, Sakai H, Imazato S. Vascularization of a Bone Organoid Using Dental Pulp Stem Cells. *Stem Cells Int*. 2023;2023:5367887.

doi: 10.1155/2023/5367887

19. Bai L, Zhou D, Li G, Liu J, Chen X, Su J. Engineering bone/cartilage organoids: strategy, progress, and application. *Bone Res*. 2024;12(1):66.

doi: 10.1038/s41413-024-00376-y

20. Deng A, Zhang H, Hu Y, *et al.* Microsphere Strategy to Generate Conformal Bone Organoid Units with Osteoimmunomodulation and Sustainable Oxygen Supply for Bone Regeneration. *Adv Sci*. 2025;12(32):e01437.

doi: 10.1002/advs.202501437

21. Huang S, Wu Y, Zhao H, *et al.* Advancements in bone organoids: perspectives on construction methodologies and application strategies. *J Adv Res*. 2026;81:745-767.

doi: 10.1016/j.jare.2025.06.011

22. Zhang H, Yan Z, Zhu J, *et al.* Extracellular Mitochondrial-Derived Vesicles Affect the Progression of Diabetic Foot Ulcer by Regulating Oxidative Stress and Mitochondrial Dysfunction. *Adv Sci*. 2025;12(10):e2407574.

doi: 10.1002/advs.202407574

23. Prieto-Vila M, Yoshioka Y, Kuriyama N, *et al.* Adult cardiomyocytes-derived EVs for the treatment of cardiac fibrosis. *J Extracell Vesicles*. 2024;13(7):e12461.

doi: 10.1002/jev2.12461

24. Liu H, Su J. Organoid and organoid extracellular vesicles for osteoporotic fractures therapy: Current status and future perspectives. *Interdiscip Med*. 2023;1(3):e20230011.

doi: 10.1002/inmd.20230011

25. Rocha S, Carvalho J, Oliveira P, *et al.* 3D Cellular Architecture Affects MicroRNA and Protein Cargo of Extracellular Vesicles. *Adv Sci*. 2018;6(4):1800948.

doi: 10.1002/advs.201800948

26. Zhou G, Li R, Sheng S, *et al.* Organoids and organoid extracellular vesicles-based disease treatment strategies. *J Nanobiotechnol*. 2024;22(1):679.

doi: 10.1186/s12951-024-02917-3

27. Morales-Sanfrutos J, Etxeberria-Ugartemendia J, Barroso-Gomila O, *et al.* Defining the reference proteomes for small extracellular vesicles and non-vesicular components. *Nat Cell Biol*. 2026;28(3):622-639.

doi: 10.1038/s41556-026-01878-z

28. Yin C, Wang X, Zhang J, *et al.* Fortified trabeculae-like biomimetic bone-filling material organoids for repair of weight-bearing bone defects. *Organoid Res*. 2026;2(2):026110016.

doi: 10.36922/OR026110016

29. Liu J, Li J, Chen Y, *et al.* Advances in bone organoids research and future perspectives. *Biofabrication*. 2025;17(4):042005.

doi: 10.1088/1758-5090/adffb9

30. de Moraes VAF, Moreira FM, Dos Santos Santinoni C, de Souza Batista VE, Mori GG. Would Exosome Therapy be Effective for Bone Regeneration? Systematic Review and Meta-Analysis. *Calcif Tissue Int*. 2025;116(1):127.

doi: 10.1007/s00223-025-01438-x

31. Goto K, Watanabe D, Yanagida K, Takagi T, Mizushima A. Harnessing miRNA-Containing Extracellular Vesicles from Mesenchymal Stromal Cell-Derived Extracellular Vesicles

for Regeneration of Bone Defects: A Narrative Review of Mechanisms, Biomaterials, and Clinical Translation. *Cancers*. 2025;17(15):2438.

doi: 10.3390/cancers17152438

32. Wu D, Qin H, Wang Z, *et al.* Bone Mesenchymal Stem Cell-Derived sEV-Encapsulated Thermosensitive Hydrogels Accelerate Osteogenesis and Angiogenesis by Release of Exosomal miR-21. *Front Bioeng Biotechnol*. 2022;9:829136.

    doi: 10.3389/fbioe.2021.829136

33. Chen Z, Bo Q, Wang C, Xu Y, Fei X, Chen R. Single BMSC-derived cartilage organoids for gradient heterogeneous osteochondral regeneration by leveraging native vascular microenvironment. *J Nanobiotechnol*. 2025;23(1):325.

    doi: 10.1186/s12951-025-03403-0

34. Lee JE, Lee YJ, Yoon JK. Advanced 3D In Vitro Liver Fibrosis Models: Spheroids, Organoids, and Liver-on-Chips. *Biomimetics*. 2025;10(10):639.

    doi: 10.3390/biomimetics10100639

35. Zhao Z, Wijerathne H, Godwin AK, Soper SA. Isolation and analysis methods of extracellular vesicles (EVs). *Extracell Vesicles Circ Nucl Acids*. 2021;2(1):80-103.

    doi: 10.20517/evcna.2021.07

36. Hao Z, Ren L, Zhang Z, *et al.* A multifunctional neuromodulation platform utilizing Schwann cell-derived exosomes orchestrates bone microenvironment via immunomodulation, angiogenesis and osteogenesis. *Bioactive Materials*. 2023;23:206-222.

    doi: 10.1016/j.bioactmat.2022.10.018

37. Wang X, Huang J, Fan W, *et al.* Lactate-binding protein DNMT3A in HRMECs promotes angiogenesis by upregulating VEGFA through HIF-1α lactylation. *Genome Biol*. 2025;26(1):377.

    doi: 10.1186/s13059-025-03845-7

38. Chen S, Lian J, Mathew R, *et al.* Vascular aging: implications, mechanisms, and interventions. *Aging Res*. 2024;2(4):9340039.

    doi: 10.26599/agr.2025.9340039

39. Saberi A, Kouhjani M, Mohammadi M, Hosta-Rigau L. Novel scaffold platforms for simultaneous induction osteogenesis and angiogenesis in bone tissue engineering: a cutting-edge approach. *J Nanobiotechnol.* 2023;21(1):351.

    doi: 10.1186/s12951-023-02115-7

40. Zhu M, Fan Z, Chen M, Xu K, Jiang Y, Su J. Biomineralization empowers bone organoids. *Biomaterials*. 2026;326:123703.

    doi: 10.1016/j.biomaterials.2025.123703

41. Ansari S, de Wildt BWM, Vis MAM, *et al.* Matrix Vesicles: Role in Bone Mineralization and Potential Use as Therapeutics. *Pharmaceuticals*. 2021;14(4):289.

    doi: 10.3390/ph14040289

42. Sheikh IA, Midura-Kiela MT, Herchuelz A, Sokolow S, Kiela PR, Ghishan FK. The Na^+/Ca^{2+} exchanger NCX3 mediates Ca^{2+} entry into matrix vesicles to facilitate initial steps of mineralization in osteoblasts. *J Extracell Vesicles*. 2024;13(6):e12450.

    doi: 10.1002/jev2.12450

43. Zhou D, Xia Z, Su J. Organoids: the future of disease modelling and therapeutics. *Biomater Transl*. 2024;5(4):335-336.

    doi: 10.12336/biomatertransl.2024.04.001

44. Chen S, Chen X, Geng Z, Su J. The horizon of bone organoid: A perspective on construction and application. *Bioact Mater*. 2022;18:15-25.

    doi: 10.1016/j.bioactmat.2022.01.048